




Complex IV subunit isoform COX6A2 protects fast-spiking interneurons from oxidative stress and supports their function

Berta Sanz-Morello¹, Ulrich Pfisterer¹, Nikolaj Winther Hansen², Samuel Demharter¹, Ashish Thakur¹, Katsunori Fujii³, Sergey A Levitskii⁴, Alexia Montalant², Irina Korshunova¹, Pradeep PA Mammen⁵, Piotr Kamenski⁴ , Satoru Noguchi^{6,7}, Blanca Irene Aldana⁸, Karin Sørig Hougaard^{9,10}, Jean-François Perrier²  & Konstantin Khodosevich^{1,*} 

Abstract

Parvalbumin-positive (PV⁺) fast-spiking interneurons are essential to control the firing activity of principal neuron ensembles, thereby regulating cognitive processes. The high firing frequency activity of PV⁺ interneurons imposes high-energy demands on their metabolism that must be supplied by distinctive machinery for energy generation. Exploring single-cell transcriptomic data for the mouse cortex, we identified a metabolism-associated gene with highly restricted expression to PV⁺ interneurons: *Cox6a2*, which codes for an isoform of a cytochrome c oxidase subunit. *Cox6a2* deletion in mice disrupts perineuronal nets and enhances oxidative stress in PV⁺ interneurons, which in turn impairs the maturation of their morphological and functional properties. Such dramatic effects were likely due to an essential role of COX6A2 in energy balance of PV⁺ interneurons, underscored by a decrease in the ATP-to-ADP ratio in *Cox6a2*^{-/-} PV⁺ interneurons. Energy disbalance and aberrant maturation likely hinder the integration of PV⁺ interneurons into cortical neuronal circuits, leading to behavioral alterations in mice. Additionally, in a human patient bearing mutations in *COX6A2*, we found a potential association of the mutations with mental/neurological abnormalities.

Keywords energy production; high-frequency firing; interneurons; oxidative stress; parvalbumin

Subject Categories Metabolism; Neuroscience

DOI 10.15252/embj.2020105759 | Received 27 May 2020 | Revised 23 June 2020 | Accepted 23 June 2020 | Published online 3 August 2020

The EMBO Journal (2020) 39: e105759

Introduction

Gamma-aminobutyric acid-containing (GABAergic) interneurons are the major source of inhibition in the mammalian brain (Hu *et al*, 2014). Parvalbumin-positive (PV⁺) interneurons are the largest class of cortical GABAergic interneurons and have been shown to regulate plasticity during learning and memory (Fishell & Rudy, 2011; Hu *et al*, 2014; Tremblay *et al*, 2016). PV⁺ interneurons are also known as fast-spiking interneurons due to their high-frequency firing, i.e., generating up to hundreds of action potentials per second, that is required to synchronize oscillations of principal neurons (Cardin *et al*, 2009; Sohal *et al*, 2009). Such generation of brain oscillations underlies sensory information processing, working memory, attention, learning, and social behavior (Hu *et al*, 2014). PV⁺ interneurons also play a major role in the regulation of the excitatory/inhibitory balance in the cortex that is often impaired in psychiatric disorders, such as schizophrenia and autism (Marin, 2012). The contribution of PV⁺ interneuron dysfunction to psychiatric disorders is highlighted by alterations in gamma oscillations in schizophrenia patients (Cho *et al*, 2006; Minzenberg *et al*, 2010) and incomplete or retarded maturation of PV⁺ interneurons in patients (Gandal *et al*, 2012) and in mouse models (Cabungcal *et al*, 2019; Vasistha *et al*, 2019).

The cellular properties of PV⁺ interneurons such as high-frequency firing, short single spikes, and fast membrane time constant must impose high-energy demands and require an elevated mitochondrial activity (Kann *et al*, 2014). Although these metabolic characteristics ensure the normal functioning of PV⁺ interneurons, they also render PV⁺ cells more sensitive to

1 Biotech Research and Innovation Centre (BRIC), Faculty of Health and Medical Sciences, University of Copenhagen, Copenhagen, Denmark

2 Department of Neuroscience, University of Copenhagen, Copenhagen, Denmark

3 Department of Pediatrics, Chiba University Graduate School of Medicine, Chiba, Japan

4 Faculty of Biology, Lomonosov Moscow State University, Moscow, Russia

5 Department of Internal Medicine, University of Texas Southwestern Medical Center, Dallas, TX, USA

6 Department of Neuromuscular Research, National Institute of Neuroscience, National Center of Neurology and Psychiatry, Tokyo, Japan

7 Medical Genome Center, National Center of Neurology and Psychiatry, Tokyo, Japan

8 Department of Drug Design and Pharmacology, University of Copenhagen, Copenhagen, Denmark

9 Section of Environmental Health, National Research Centre for the Working Environment, Copenhagen, Denmark

10 Department of Public Health, University of Copenhagen, Copenhagen, Denmark

*Corresponding author. Tel: +45 353 32533; E-mail: konstantin.khodosevich@bric.ku.dk

oxidative stress (Kann, 2016). Indeed, genetic and pharmacological manipulations of the redox system lead to alterations in PV⁺ interneurons that do not affect other types of neurons (Cabungcal *et al*, 2019). The high vulnerability of PV⁺ interneurons to oxidative stress has been also demonstrated in a number of genetic and environmental animal models of mental disorders (Steullet *et al*, 2017). Such vulnerability to oxidative stress, which is especially pronounced during brain maturation (Behrens & Sejnowski, 2009), could lead to a selective dysfunction of PV⁺ interneurons in mental disorders (Chung *et al*, 2016; Steullet *et al*, 2017; Vasistha *et al*, 2019). Therefore, in the healthy brain, PV⁺ interneurons must benefit from an optimized metabolism accounting for their high-energy demands, which simultaneously preserve their cellular properties and protect them against oxidative stress. However, in spite of being one of the most studied neurons in the brain, it is still unknown how PV⁺ interneurons sustain energy demands for high-frequency firing.

Since the main source of energy in neurons is oxidative phosphorylation (Sokoloff, 1960), PV⁺ interneurons might have optimized the oxidative phosphorylation machinery to produce ATP according to their demands. To test this, we leveraged single-cell (sc) transcriptomic data to cross-compare the expression of metabolic genes between PV⁺ interneurons and all other types of neurons in the mouse cortex. We observed that one gene, *Cox6a2*, showed highly specific expression in PV⁺ interneurons. *Cox6a2* codes for the isoform 2 of the subunit COX6A, which integrates cytochrome *c* oxidase, also known as complex IV (CIV), in the oxidative phosphorylation pathway (Kadenbach *et al*, 1982). We showed that the specific expression of *Cox6a2* in PV⁺ interneurons in the brain is highly conserved across mammals. *Cox6a2*^{-/-} PV⁺ interneurons exhibit reduced expression of parvalbumin and a lower number of synaptic contacts onto principal neurons. Furthermore, *Cox6a2*^{-/-} increases oxidative stress in PV⁺ interneurons and decreases the density of the perineuronal nets (PNNs) surrounding these cells, which in turn can affect the function of the local cortical circuits. Indeed, the maturation of the functional and morphological properties of *Cox6a2*^{-/-} PV⁺ interneurons is perturbed, and *Cox6a2*^{-/-} mice exhibit behavioral alterations associated with hyperactivity. Altogether, we show that COX6A2 is essential for the proper maturation and function of PV⁺ interneurons and *Cox6a2* deletion disrupts the unique cellular properties of fast-spiking interneurons leading to behavioral abnormalities.

Results

Identification of genes associated with energy production that are enriched in PV⁺ interneurons

To identify genes that might contribute to sustain the high metabolic demands of PV⁺ interneurons, we explored the sc transcriptomic dataset produced for the mouse visual cortex (Tasic *et al*, 2016). For each cell type, we compared the expression of genes belonging to the gene ontology (GO) term: 0006091 “generation of precursor metabolites and energy”, 358 genes in total (Appendix Fig S1). Several genes were detected in PV⁺ interneurons but were largely absent in other cell types. In particular, the expression of *Cox6a2* was found to be highly restricted to PV⁺ interneurons, showing a

very scarce expression in other types of interneurons and virtually no expression in principal neurons and glial cells (Fig 1A).

Cox6a2 expression is highly specific to PV⁺ interneurons in the mammalian brain

Cox6a2 codes for one of the two isoforms of the COX6A subunit, which belongs to CIV in the electron transport chain. COX6A2 (also known as COX6A heart-type or COX6AH) has been previously detected only in the heart and skeletal muscle (Kadenbach *et al*, 1982; Taanaman *et al*, 1993). COX6A2 can bind ADP, which leads to an increase in the catalytic activity of CIV, indicating that COX6A2-containing CIV can respond to rises in the ATP-to-ADP ratio within the mitochondria (Anthony *et al*, 1993; Frank & Kadenbach, 1996). The other protein isoform of COX6A, COX6A1, is ubiquitously expressed in the organism (Taanaman *et al*, 1993; Grossman *et al*, 1995), and we confirmed its presence in all brain cells by analyzing the sc transcriptomic dataset for the mouse visual cortex (Tasic *et al*, 2016) (Fig 1A). Importantly, COX6A1 does not interact with ADP, and thus, COX6A1-containing CIV cannot modulate its own activity by sensing changes in the ATP-to-ADP ratio (Anthony *et al*, 1993; Frank & Kadenbach, 1996). Therefore, COX6A2 and COX6A1 isoforms show remarkable functional differences.

Since previous studies failed to detect COX6A2 mRNA and protein in the rodent brain, we sought to support the transcriptomic results by additional approaches. Using cortical tissue from mouse brain, we demonstrated the presence of COX6A2 mRNA by reverse transcription polymerase chain reaction (RT-PCR) and COX6A2 protein by Western blot analysis (Fig 1B and C). We next confirmed by immunohistochemistry that COX6A2 is almost exclusively expressed in PV⁺ interneurons in the adult mouse brain, including the cortex, hippocampus, and striatum (Fig 1E–J). Specific expression of COX6A2 in cortical PV⁺ interneurons was also previously indicated by *in situ* hybridization in a recent study (Mancarci *et al*, 2017), and previous sc transcriptomic studies identified specific COX6A2 expression in cortical (Paul *et al*, 2017) and striatal (Muñoz-Manchado *et al*, 2018) PV⁺ interneurons. Together with somatostatin-expressing (SST⁺) and serotonin 3A receptor-expressing (5HT3AR⁺) interneurons, PV⁺ interneurons represent one of the three major classes of GABAergic interneurons in the cortex and account for ~40% of all GABAergic interneurons (Rudy *et al*, 2011). Accordingly, we found that 38% of GAD67-expressing (GAD67⁺) interneurons in the cortex of GAD67-EGFP knock-in mice (Tamamaki *et al*, 2003) co-express *Cox6a2* (Fig EV1A and B). Moreover, COX6A2 is almost absent in the other two major classes of cortical interneurons, being detected in 3% of 5HT3AR⁺ interneurons in 5HT3AR-EGFP transgenic mice (Fig EV1C and D) and in 3.5% of SST⁺ interneurons in GIN transgenic mice (Fig EV1E and F).

The expression of *Cox6a2* commences in the cortex at postnatal day 0 (P0) and rises until P60 (Fig 1D). Immunohistochemistry analyses revealed that COX6A2 immunoreactivity becomes evident at P9 (Fig 1K). Once parvalbumin expression is detectable at P13, COX6A2 is almost exclusively localized in PV⁺ interneurons (Fig 1L–N). To analyze whether *Cox6a2* selective expression in PV⁺ interneurons is conserved from rodents to humans, we co-labeled COX6A2 and PV in the cortex of rat, rhesus monkey, and human.

Similarly to the results observed in the mouse brain, we found that COX6A2 is detected almost exclusively in PV⁺ interneurons in the cortex of adult rat and adult rhesus monkey (Fig 2A–D). In the adult human brain, all cortical PV⁺ interneurons from Brodmann areas 9 and 10 (BA9, BA10), which correspond to the dorsolateral and medial prefrontal cortex and the anterior prefrontal cortex, respectively, express COX6A2, and PV⁺ interneurons represent 60% of the cells expressing COX6A2 (Fig 2E and F).

To investigate how the restricted expression of *Cox6a2* in PV⁺ interneurons in mammals might be regulated, we cross-compared *Cox6a2* promoter sequences from different species searching for putative, conserved transcription factor binding sites. We identified two E-box and one MEF2-binding sites that were highly conserved across the genomes of mouse, rat, rhesus monkey, and human (Fig EV2A). To determine the implication of these sites in the regulation of *Cox6a2* expression, we injected into the mouse

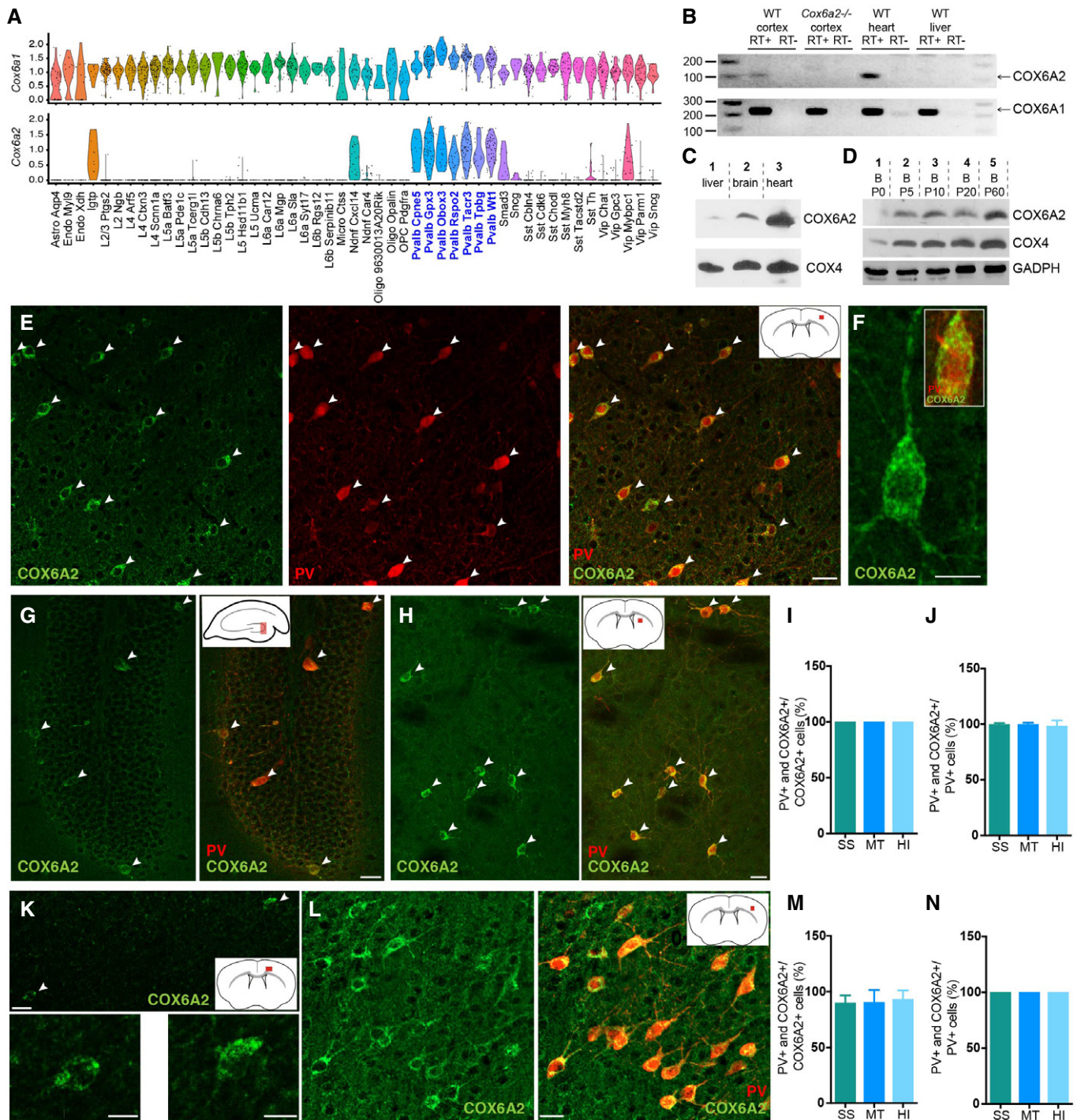


Figure 1.

Figure 1. *Cox6a2* expression is restricted to PV⁺ interneurons in the mouse brain.

A Analysis of the single-cell transcriptomic dataset for the mouse visual cortex (Tasic et al, 2016) revealed that the expression of the metabolism-associated gene *Cox6a2* is highly restricted to PV⁺ interneurons. *Cox6a2* is expressed in all subtypes of PV⁺ interneurons (marked in blue color) but rarely detected in other neuronal subtypes from the mouse visual cortex. *Cox6a1*, which encodes the other protein isoform of COX6A, is expressed in all subtypes.

B, C RT-PCR and Western blot, respectively, showing expression of *Cox6a2* in the brain and heart.

D Western blot analysis showed that COX6A2 is first detected in the brain at postnatal day 0 (P0). Then, COX6A2 protein levels gradually increase until P60.

E–H COX6A2 immunoreactivity is detected in PV⁺ interneurons in different brain areas of adult mice, including the cortex (general overview in E and single PV⁺ interneuron magnification in F), hippocampus (G), and striatum (H). White arrowheads indicate PV/Cox6a2 double-positive cells.

I, J Quantifications showing almost 100% of co-localization of COX6A2⁺ cells and PV⁺ cells in the somatosensory (SS) and motor (MT) cortices, and the hippocampus (HI) of adult mice (*n* animals = 4, 2 months old, *n* sections = 24 SS, 16 MT, 8 HI).

K COX6A2 immunoreactivity in the cortex at P9 (*n* animals = 2, *n* sections = 12 SS, 8 MT, 4 HI). White arrowheads indicate Cox6a2-positive cells.

L–N As soon as parvalbumin immunoreactivity becomes visible at P13, almost 100% of PV⁺ cells are co-labeled with COX6A2 immunoreactivity in the SS and MT cortices, and the HI of P13 mice (*n* = 2).

Data information: All error bars represent SD. In all quantifications, the data are shown per section analyzed. Scale bars: 20 μm (E, G, H, K, L) and 10 μm (F, K inset). COX4: cytochrome c oxidase subunit 4; GAPDH: glyceraldehyde 3-phosphate dehydrogenase.

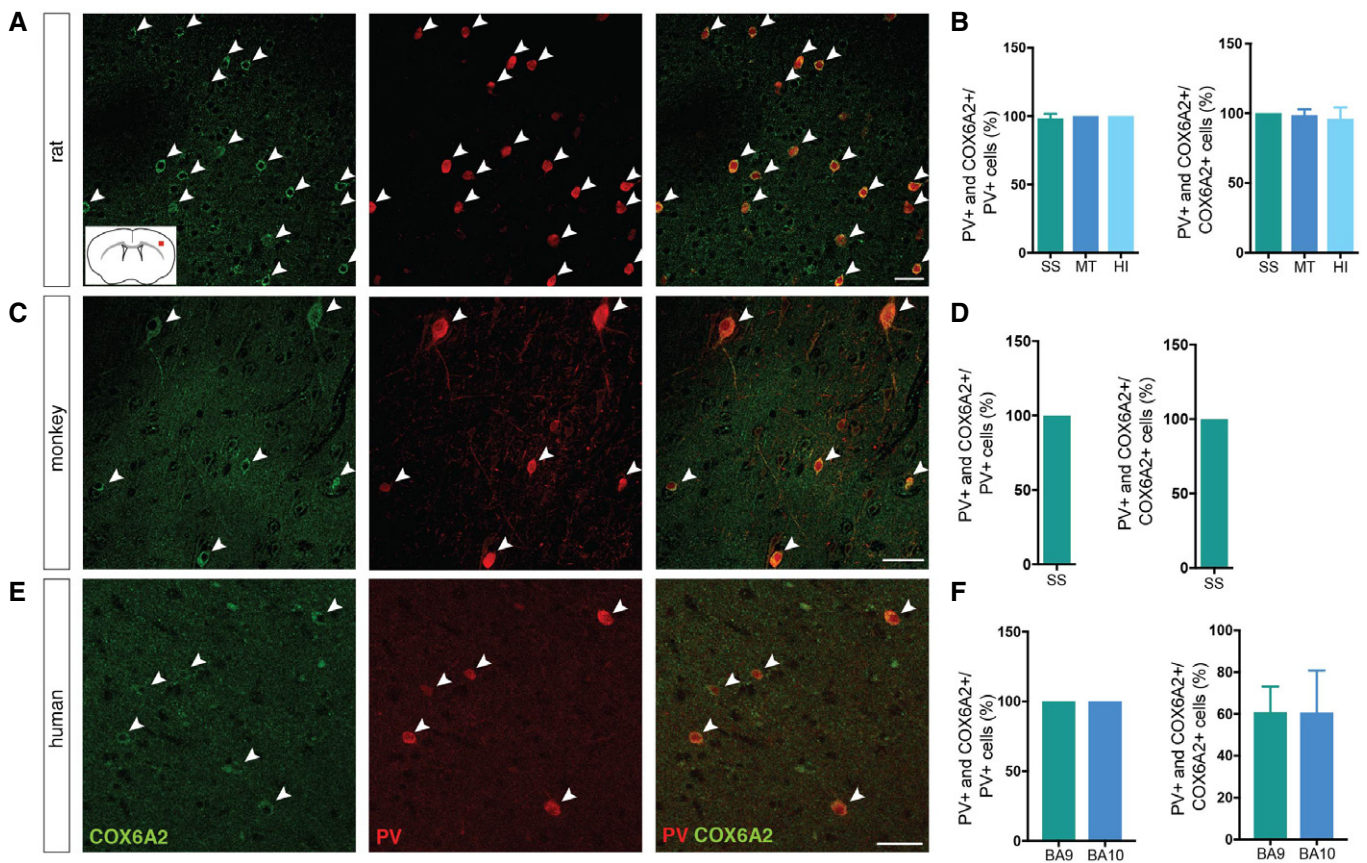


Figure 2. *Cox6a2* expression in PV⁺ interneurons is conserved from rodents up to humans.

A, B COX6A2 immunoreactivity is virtually restricted to PV⁺ interneurons in the somatosensory (SS) and motor (MT) cortices, and the hippocampus (HI) of adult rat (*n* animals = 1, 2.5 months old, *n* sections = 12 SS, 8 MT, 4 HI). White arrowheads indicate PV/Cox6a2 double-positive cells.

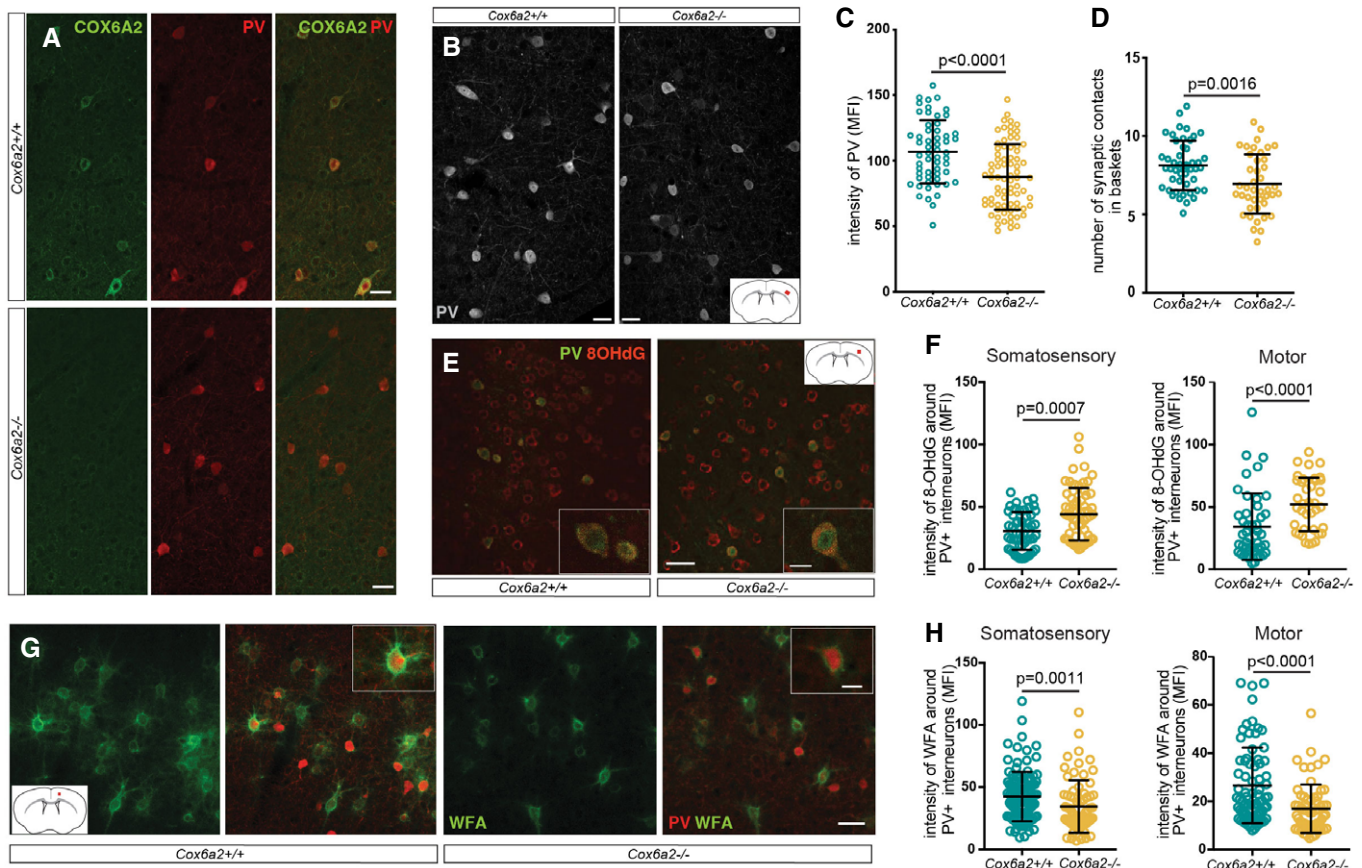
C, D In the SS cortex of adult rhesus monkey, COX6A2 immunoreactivity is present exclusively in PV⁺ cells (*n* animals = 1, 1 year old, *n* sections = 6). White arrowheads indicate PV/Cox6a2 double-positive cells.

E, F In adult humans, all cortical PV⁺ interneurons from Brodmann areas 9 and 10 (BA9 and BA10) are co-labeled with COX6A2 immunoreactivity. However, PV⁺ interneurons represent 60% of the cells in which COX6A2 is detected (*n* human subjects = 2, 59 and 69 years old, *n* sections = 6 BA9, 6 BA10). White arrowheads indicate PV/Cox6a2 double-positive cells.

Data information: All error bars represent SD. In all quantifications, the data are shown per section analyzed. Scale bars: 50 μm (A, C, E).

cortex adeno-associated viruses (AAVs) expressing EGFP under the control of a short version of the native or mutated *Cox6a2* promoter containing point mutations in the E-box2- or MEF2-

binding sites (Fig EV2B). Although short promoters do not provide full specificity due to lack of upstream/downstream regulatory sequences, we showed that the native short promoter



ensured relatively high specificity of EGFP expression in PV⁺ interneurons, whereas the specificity was decreased for mutated promoters (Fig EV2C and D), indicating that both sites are involved in regulation of *Cox6a2* expression. We predicted E-box-binding factors that might regulate *Cox6a2* expression in PV⁺ interneurons by searching through the sc transcriptomic dataset for the mouse visual cortex (Tasic *et al*, 2016) for the expression of genes in the GO Term: 0070888 “E-box binding”. Robust expression of 22 E-box-binding factors was found in PV⁺ interneurons, of which nine had preferential expression in PV⁺ interneurons (Fig EV2E, marked green), possibly accounting for the specificity of *Cox6a2* expression.

***Cox6a2* knockout increases oxidative stress in PV⁺ interneurons and disrupts the perineuronal nets surrounding them**

Although currently the function of COX6A2 in the brain is unknown, studies in the heart and skeletal muscle, where COX6A2 is also expressed, have suggested that COX6A2 is necessary to control the activity of the electron transport chain and to protect against abnormal reactive oxygen species (ROS) generation (Quintens *et al*, 2013). Thus, we utilized *Cox6a2*^{-/-} mice (Radford *et al*, 2002) to determine the role of COX6A2 in the development and function of PV⁺ interneurons. As expected, *Cox6a2* expression was absent in the cortex of adult *Cox6a2*^{-/-} mice (Fig 3A). We found that

Cox6a2^{-/-} had negligible effect on the density and distribution of PV⁺ interneurons in the cortex at ~P60 and ~P180 (Fig EV3A–D). However, *Cox6a2*^{-/-} led to decreased parvalbumin expression in PV⁺ interneurons (Fig 3B and C), which might affect PV⁺ interneurons activity, given the role of parvalbumin as a calcium buffer (Caillard *et al*, 2000). Decrease in parvalbumin expression was also reported in mouse models of mental disorders (Mukherjee *et al*, 2019; Patrizi *et al*, 2020) and human patients (Enwright *et al*, 2016). Furthermore, *Cox6a2*^{-/-} reduced the number of PV⁺ interneuron-derived synaptic contacts onto cortical principal neurons (Fig 3D), which might indicate impaired connectivity between PV⁺ interneurons and principal neurons.

Naturally, fast-spiking properties of PV⁺ interneurons impose high metabolic demands and there is a higher density of mitochondria (Gulyas *et al*, 2006), which makes this cell type particularly vulnerable to oxidative stress (Cabungcal *et al*, 2013a). Enhanced oxidative stress, which can be also associated with impaired metabolism or energy generation, was shown to be a common defect of PV⁺ interneurons in mental disorders (Steullet *et al*, 2017; Cabungcal *et al*, 2019). Thus, we measured the level of oxidative stress by quantifying the fluorescence intensity of 8-hydroxy-2'-deoxyguanosine (8OHdG), a marker of oxidative DNA damage, in PV⁺ interneurons from the somatosensory and motor cortices of wild-type (WT) and *Cox6a2*^{-/-} mice (Fig 3E). We observed a dramatic increase in the fluorescence intensity of 8OHdG labeling in *Cox6a2*^{-/-} PV⁺ interneurons in both cortices, indicating that *Cox6a2*^{-/-} PV⁺ interneurons exhibit a large upregulation of oxidative stress (Fig 3F). A great number of PV⁺ interneurons are enwrapped in PNNs that are extracellular matrix structures stabilizing their synapses and protecting against oxidative stress (Cabungcal *et al*, 2013b). To investigate whether the upregulation of oxidative stress correlates with the effect of *Cox6a2*^{-/-} on PNNs, we stained PNNs using *Wisteria floribunda* agglutinin (WFA) and measured WFA fluorescence intensity around PV⁺ cells (Fig 3G). *Cox6a2*^{-/-} mice exhibited a large decrease in the fluorescence intensity of WFA around PV⁺ interneurons in both motor and somatosensory cortices (Fig 3H), thus correlating with the increased rate of oxidative stress in these areas. Since reduced density of PNNs and increased oxidative stress in PV⁺ interneurons have been observed in mouse models of mental disorders and human patients (Cabungcal *et al*, 2013b; Enwright *et al*, 2016; Steullet *et al*, 2017; Wen *et al*, 2018; Lovelace *et al*, 2020), *Cox6a2* expression might be necessary for the normal function of PV⁺ interneurons by supporting PNNs and diminishing oxidative stress in PV⁺ interneurons.

Alterations in molecular signaling in PV⁺ interneurons lacking *Cox6a2*

To elucidate the molecular mechanisms that are associated with *Cox6a2*^{-/-} and might underlie the observed changes in oxidative stress, we compared the transcriptome of WT and *Cox6a2*^{-/-} PV⁺ interneurons. To this end, we sorted PV⁺ interneurons from *Cox6a2*^{-/-} and WT PV-EGFP (Meyer *et al*, 2002) mice and compared their transcriptome by RNA sequencing. We found that a number of genes implicated in cellular metabolism, oxidative stress response, and synaptic transmission were dysregulated in *Cox6a2*^{-/-} PV⁺ interneurons (Fig 4A and Appendix Tables S1

and S2). Interestingly, not only *Cox6a2* transcription was completely abolished in *Cox6a2*^{-/-} PV⁺ interneurons, but also *Cox6a1* showed decreased expression (Fig 4B), which might further affect oxidative phosphorylation in *Cox6a2*^{-/-} PV⁺ interneurons. In addition, we detected a reduced expression of parvalbumin (*Pvalb*; Fig 4B), which confirmed our previous immunohistochemistry results. Both glutamate decarboxylase 1 (*Gad1*) and 2 (*Gad2*) genes also exhibited a reduced expression (Fig 4B), which might lead to a lower rate of GABA synthesis and, as a result, diminished potential for inhibition by *Cox6a2*^{-/-} PV⁺ interneurons.

As expected, *Cox6a2* deletion led to a dramatic dysregulation of the oxidative stress-response machinery (Fig 4C), thus confirming our immunohistochemistry data and suggesting that the activation of a homeostatic response counteracts the increased oxidative stress detected in *Cox6a2*^{-/-} PV⁺ interneurons. Importantly, we found a profound dysregulation in the expression of AMPA receptor genes, genes coding for sodium and potassium channels, and intracellular calcium signaling proteins (Fig 4C), which most probably underlie the electrophysiological alterations observed in *Cox6a2*^{-/-} PV⁺ interneurons.

Finally, we explored pathways that were modulated in *Cox6a2*^{-/-} PV⁺ interneurons by searching for enriched GO terms in the top 200 up/downregulated genes. Interestingly, we found a prominent upregulation of immune response-related pathways in *Cox6a2*^{-/-} PV⁺ interneurons (Fig 4D and Appendix Table S3), which might be due to genetic/epigenetic alterations caused by increased oxidative stress. Importantly, the pathways controlling ion channel and receptor activity were markedly downregulated in *Cox6a2*^{-/-} PV⁺ interneurons (Fig 4D and Appendix Table S3), which might lead to impairments in the cellular properties and function of *Cox6a2*^{-/-} PV⁺ interneurons. In addition, we detected an upregulation of cytoskeleton-associated pathways (Fig 4D and Appendix Table S3), further underlying likely disturbances in the functional and morphological maturation of *Cox6a2*^{-/-} PV⁺ interneurons.

COX6A2 regulates energy balance in PV⁺ interneurons

We next sought to provide a direct proof that COX6A2 is necessary for energy generation in PV⁺ interneurons. Previous studies in the heart have shown that COX6A2 can bind ADP, which increases the catalytic activity of CIV. Therefore, COX6A2-containing CIV is able to respond to drops in mitochondrial ATP-to-ADP ratio (Anthony *et al*, 1993; Frank & Kadenbach, 1996). To elucidate the role of COX6A2 in energy generation of PV⁺ interneurons, we performed live-cell imaging of the ATP-to-ADP ratio using the genetically encoded fluorescent biosensor PercevalHR (Tantama *et al*, 2013). We generated a transgenic mouse line, where the first exon of *Cox6a2* is flanked by loxP sites (see Methods and Appendix Fig S2) and crossed the mice with the PV-CRE mouse line (Hippenmeyer *et al*, 2005) for conditional knockout of *Cox6a2* in PV⁺ interneurons by CRE recombinase (Fig 5A). We infected the somatosensory cortex of *Cox6a2*^{fl/fl};PV-CRE and *Cox6a2*^{+/+};PV-CRE mice with AAV that expressed PercevalHR in a FLEX vector, where the gene was flanked by loxP sites that are recognized by CRE recombinase and turn on PercevalHR expression only upon CRE recombination (Fig 5A). This strategy allowed us to selectively express PercevalHR in PV⁺ interneurons. After several weeks, which ensured

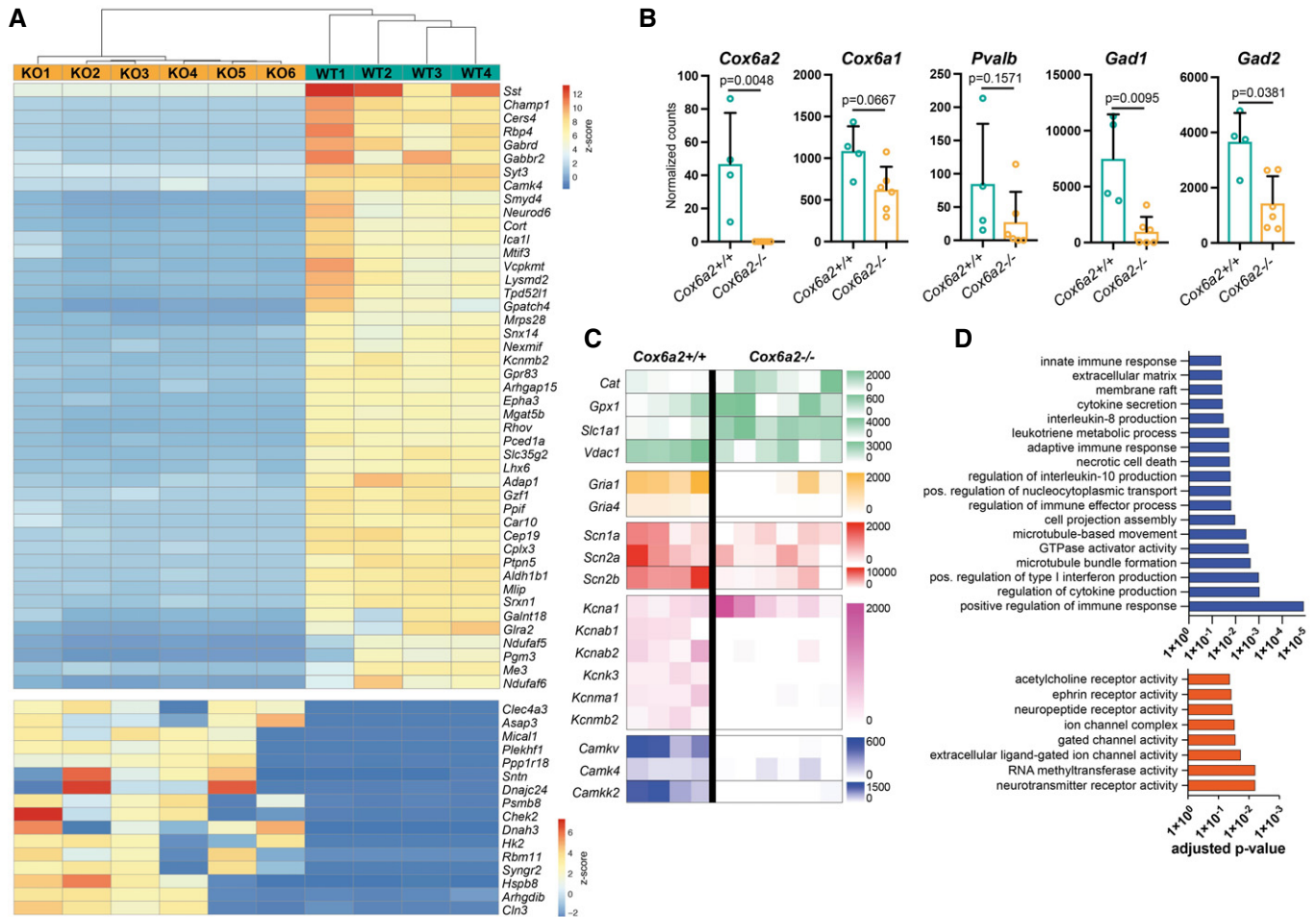


Figure 4. Intracellular signaling in PV⁺ interneurons is affected by *Cox6a2* knockout.

A PV⁺ interneurons were sorted from cortices of PV-EGFP WT and *Cox6a2*^{-/-} mice at P15 and processed for bulk RNA sequencing ($n = 4$ WT, 6 *Cox6a2*^{-/-}; P15). Heat map shows expression for top downregulated (red) and upregulated (blue) genes in *Cox6a2*^{-/-} PV⁺ interneurons relative to their WT counterparts.

B *Cox6a2* expression was effectively abolished in *Cox6a2*^{-/-} PV⁺ interneurons. In addition, *Cox6a2* knockout led to a decreased expression of *Gad1* and *Gad2* genes ($n = 4$ WT, 6 *Cox6a2*^{-/-}). Two-tailed unpaired Mann–Whitney tests.

C Changes in expression of oxidative stress-related genes (green), genes coding for AMPA receptors (orange), sodium channels (red), potassium channels (magenta), and internal calcium signaling proteins (blue). Color scale bars show normalized read counts.

D Significantly downregulated (red) and upregulated (blue) gene ontology (GO) terms based on top 200 downregulated/upregulated genes in *Cox6a2*^{-/-} PV⁺ interneurons (Benjamini–Hochberg-adjusted P -values). See also Appendix Tables S1–S3. For detailed statistical information, see Appendix Table SSE.

Data information: All error bars represent SD.

appropriate protein levels of PercevalHR in PV⁺ interneurons, we performed *ex vivo* recordings of PercevalHR fluorescence in brain slices using 2-photon microscopy (Fig 5B). PercevalHR is a ratio-metric fluorescent protein that changes its excitation spectrum based on its binding to ATP (930 nm) or ADP (840 nm) and provides an estimate of the ATP-to-ADP ratio within the cell (Fig 5C) (Tantama *et al*, 2013). We showed that in basal conditions PV⁺ interneurons from WT mice exhibit dramatically higher ATP-to-ADP ratio than PV⁺ interneurons from conditional *Cox6a2*^{-/-} mice (Fig 5D and E). These results demonstrate that the presence of COX6A2-containing CIV in PV⁺ interneurons gives rise to higher ATP-to-ADP ratio that possibly ensures the generation of adequate levels of energy to maintain the characteristic electrophysiological properties of fast-spiking interneurons.

***Cox6a2* knockout alters the functional and morphological maturation of PV⁺ interneurons**

Since *Cox6a2* starts to be expressed early postnatally and *Cox6a2*^{-/-} PV⁺ interneurons exhibit dramatic changes in their transcriptome, we explored the impact of *Cox6a2*^{-/-} on the development of PV⁺ interneuron cellular properties and firing activity by electrophysiological analysis. To this end, we recorded PV⁺ interneurons residing in the somatosensory cortex of P22–P45 *Cox6a2*^{-/-} and WT PV-EGFP mice. This time window corresponds to the late maturational period of PV⁺ interneurons (Okaty *et al*, 2009; Miyamae *et al*, 2017). The electrophysiological maturation of PV⁺ interneurons was evaluated either by comparing the maturational dynamics across the whole period under study (i.e., P22–P45) or by splitting it

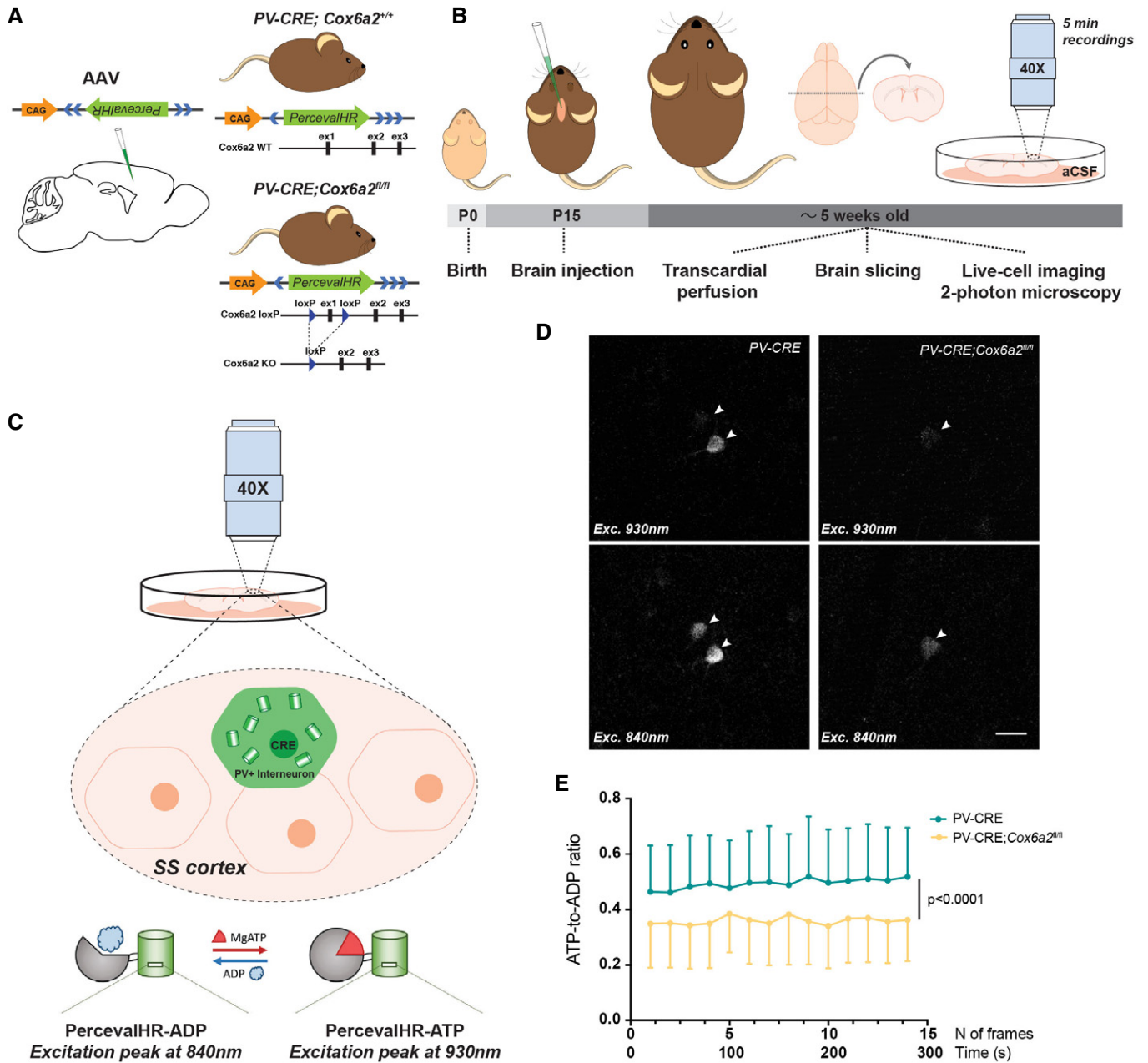


Figure 5. Ex vivo live-cell imaging shows that COX6A2 regulates energy balance in PV⁺ interneurons.

A Experimental scheme. The selective expression of CRE recombinase in PV-CRE and PV-CRE;Cox6a2^{fl/fl} mice ensures the expression of PercevalHR only in PV⁺ interneurons.
B Experiment timeline. AAVs expressing PercevalHR were injected in the somatosensory (SS) cortex of mice at postnatal day 15 (P15). Approximately 3 weeks after the injections, the brains were sliced into coronal sections for live-cell imaging of ATP-to-ADP ratio by 2-photon microscopy.
C PercevalHR is a ratiometric fluorescent protein that changes its excitation spectrum based on its binding to ATP (930 nm) or ADP (840 nm).
D Representative images of PV⁺ interneurons from PV-CRE and PV-CRE;Cox6a2^{fl/fl} mice showing PercevalHR fluorescence after excitation at 930 and 840 nm. White arrowheads indicate PercevalHR-expressing cells. Scale bar: 20 μm.
E PV⁺ interneurons from PV-CRE;Cox6a2^{fl/fl} mice exhibited significantly lower ATP-to-ADP ratio than PV⁺ interneurons from PV-CRE mice throughout the entire duration of the recordings (23 cells from 4 PV-CRE mice; 15 cells from 6 PV-CRE;Cox6a2^{-/-} mice). Data were analyzed by two-way ANOVA. Error bars represent SD.

into two equal parts. Thus, PV⁺ interneurons were grouped into P22–P33 (24 WT PV⁺ interneurons, 14 Cox6a2^{-/-} PV⁺ interneurons) and P34–P45 periods (15 WT PV⁺ interneurons, 29

Cox6a2^{-/-} PV⁺ interneurons), since the major maturation of GABAergic interneurons is largely finished by ~P30–P35 (reviewed in Le Magueresse & Monyer, 2013); for PV⁺ interneurons, see, e.g.,

(Lu et al, 2014)), whereas few other parameters such as parvalbumin expression and enwrapping by PNNs continue to be changed after P30 up to P60 (Patrizi et al, 2020). Although *Cox6a2*^{-/-} did not affect the resting membrane potential (V_{rest}) and spike amplitude in PV⁺ interneurons (Fig 6A and B), *Cox6a2*^{-/-} and WT PV⁺ interneurons differed in the threshold for action potentials, which increased during maturation in WT, but such maturational increase was abolished in *Cox6a2*^{-/-} PV⁺ neurons (Fig 6C and D). Consequently, the threshold was significantly more negative for *Cox6a2*^{-/-} than for WT PV⁺ interneurons during the later stage of maturation (Fig 6C and D). These data suggest that older *Cox6a2*^{-/-} PV⁺ interneurons reach the threshold for action potentials more easily than WT PV⁺ interneurons and thus might be more excitable.

Since knocking out *Cox6a2* might impair the high-frequency firing pattern of PV⁺ interneurons due to dysregulation of energy generation, we tested the ability of PV⁺ interneurons to fire repetitively in response to 2-s depolarizing current pulses. At P22-P33, we

found that the difference between the amplitude of the first 10 and the last 10 action potentials of the train was similar in both groups (Fig 6E and F). However, whereas at P34-P45 the amplitude difference in WT PV⁺ interneurons was lower than that observed in younger WT PV⁺ cells, underlying their proper maturation (Fig 6E and F), in *Cox6a2*^{-/-} PV⁺ interneurons the amplitude difference did not change from P22-33 to P34-45, again indicating impairment in maturation of the functional properties of *Cox6a2*^{-/-} PV⁺ interneurons (Fig 6E and F). These data suggest that, in spite of their higher excitability, PV⁺ interneurons from *Cox6a2*^{-/-} mice have difficulties to sustain repetitive firing. To confirm this hypothesis, we measured the maximal firing frequency that could be reached by PV⁺ interneurons by increasing the amplitude of current pulses. We observed that while WT PV⁺ interneurons increased the maximal firing frequency with maturation, such maturational increase was abolished in *Cox6a2*^{-/-} interneurons (Fig 6G). Together, these results demonstrate striking alterations in the electrophysiological

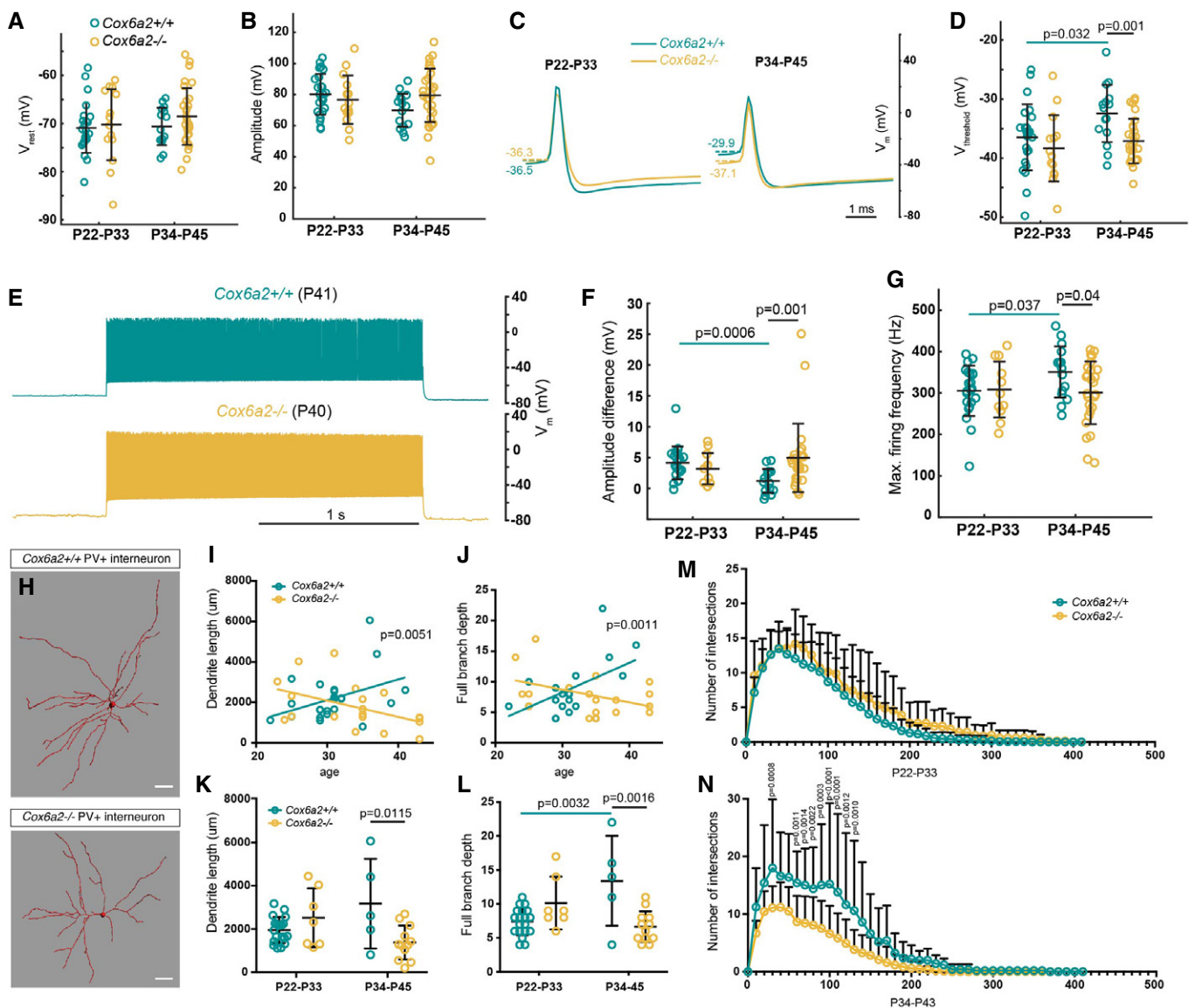


Figure 6.

Figure 6. *Cox6a2* knockout in PV⁺ interneurons delays their functional and morphological maturation.

- A, B The resting membrane potential and amplitude of action potentials in WT and *Cox6a2*^{-/-} PV⁺ interneurons, respectively. Two-tailed unpaired Student's *t*-tests.
- C, D The threshold for action potentials increased over maturation in WT but not in *Cox6a2*^{-/-} PV⁺ interneurons. As a result, the threshold for action potentials was significantly lower in P34–45 *Cox6a2*^{-/-} PV⁺ interneurons when compared to their WT counterparts. (D) Two-tailed unpaired Student's *t*-tests.
- E, F Trains of action potentials were evoked by 2-s depolarizing current pulses. The amplitude difference (difference between the mean amplitude of 1st–10th action potentials and 190th–200th action potentials) was significantly higher in P34–45 *Cox6a2*^{-/-} compared with WT PV⁺ interneurons. In addition, the amplitude difference decreased with maturation in WT but not in *Cox6a2*^{-/-} PV⁺ interneurons. (F) Two-tailed unpaired Mann–Whitney tests.
- G While in WT PV⁺ interneurons the maximal firing frequency increased during maturation, such increase was abolished by *Cox6a2* knockout. Thus, maximal firing frequency reached during 2-s depolarizing current pulses was lower in P34–45 *Cox6a2*^{-/-} compared with WT PV⁺ interneurons. Two-tailed unpaired Student's *t*-tests.
- H Recorded PV⁺ interneurons were filled with biocytin, and their dendritic morphology was reconstructed using Imaris software. Scale bars: 30 μm.
- I, J *Cox6a2*^{-/-} PV⁺ interneurons showed a negative correlation between age and dendritic length and between age and full branch depth (maximal number of branches between the soma and a terminal dendritic point), which contrasted with the expected positive correlation between these parameters in WT PV⁺ interneurons. Linear regression of Pearson's correlation.
- K, L WT and *Cox6a2*^{-/-} PV⁺ interneurons showed similar values for dendritic length and full branch depth at P22–P33. However, at P34–P45, *Cox6a2*^{-/-} PV⁺ interneurons showed lower dendritic length and full branch depth than WT PV⁺ interneurons. Two-way ANOVA followed by Tukey's multiple comparisons tests.
- M, N While younger WT and *Cox6a2*^{-/-} PV⁺ interneurons have similar dendritic tree complexities (M), at the later stage of maturation *Cox6a2*^{-/-} PV⁺ interneurons show a reduction in dendritic tree complexity in comparison with WT PV⁺ interneurons (N). Multiple *t*-tests, two-stage step-up method of Benjamini, Krieger, and Yekutieli.
- Data information: For amplitude and maximal firing frequency, *n* = 37 WT (*n* = 22 P22–P33, *n* = 15 P34–P45) and 37 *Cox6a2*^{-/-} (*n* = 11 P22–P33, *n* = 26 P34–P45) PV⁺ interneurons. For the rest of the electrophysiological parameters analyzed, *n* = 39 WT (*n* = 24 P22–P33, *n* = 15 P34–P45) and 43 *Cox6a2*^{-/-} (*n* = 14 P22–P33, *n* = 29 P34–P45) PV⁺ interneurons. For all morphological comparisons, *n* = 24 WT (*n* = 19 P22–P33, *n* = 5 P34–P45) and 19 *Cox6a2*^{-/-} (*n* = 7 P22–P33, *n* = 12 P34–P45) PV⁺ interneurons. All error bars represent SD. For detailed statistical information, see Appendix Table S5F–H.

properties of PV⁺ interneurons during maturation, which could lead to severe dysregulation of cortical network activity.

To investigate whether the impaired electrophysiological maturation of *Cox6a2*^{-/-} PV⁺ interneurons correlates with morphological abnormalities, we reconstructed and analyzed the dendritic arborizations of *Cox6a2*^{-/-} PV⁺ interneurons upon biocytin filling (Fig 6H). Strikingly, we observed a negative correlation between age and dendritic length and between age and full branch depth in *Cox6a2*^{-/-} PV⁺ interneurons, which contrasts with the normal maturation profile of WT PV⁺ interneurons, where a continuous increase in the dendritic length and branching was observed over time (Fig 6I and J). To further analyze how *Cox6a2* deletion affects morphology during maturation, we compared changes in the dendrites of *Cox6a2*^{-/-} and WT PV⁺ interneurons across two maturation periods (P22–P33 and P34–P45), as we did for electrophysiology. We found that although the dendritic length was similar for WT and *Cox6a2*^{-/-} PV⁺ interneurons at P22–P33, it was significantly lower for *Cox6a2*^{-/-} PV⁺ interneurons at P34–P45 (Fig 6K). Similarly, the full branch depth was comparable between the genotypes at P22–P33, but lower for *Cox6a2*^{-/-} PV⁺ interneurons at P34–P45 (Fig 6L). Finally, we found a significant decrease in the dendritic tree complexity of *Cox6a2*^{-/-} relative to WT PV⁺ interneurons at P34–P45, but not before (Fig 6M and N). Overall, *Cox6a2*^{-/-} PV⁺ interneurons exhibit morphological and physiological alterations that appear during late maturation. Such alterations should affect cortical circuits, possibly leading to behavioral abnormalities in *Cox6a2*^{-/-} mice.

***Cox6a2*^{-/-} mice exhibit behavioral alterations**

We next investigated whether the physiological and morphological abnormalities observed in PV⁺ interneurons from *Cox6a2*^{-/-} mice lead to behavioral alterations. Therefore, we subjected *Cox6a2*^{-/-} and WT female mice to a battery of tests that included the open-field test (OFT, Fig 7A), social interaction test (SIT, Fig 7C), and prepulse inhibition (PPI) of the acoustic startle response test

(Fig 7E). In the OFT and SIT, *Cox6a2*^{-/-} mice exhibited increased locomotor activity since they traveled longer distances and they did so faster than WT mice (Fig 7B and D). Additionally, *Cox6a2*^{-/-} mice moved more frequently from the outer zone to the inner zone of the arena (Fig 7B and D). These findings indicate that female *Cox6a2*^{-/-} mice are hyperactive. In the SIT, both *Cox6a2*^{-/-} and WT mice preferred to spend more time interacting with a stranger mouse than with an inanimate object (Fig 7D). Although overall the startle responses to the presentation of a loud stimulus (120 dB) alone or preceded by a prepulse stimulus were similar between both groups, they were significantly lower in *Cox6a2*^{-/-} mice when the 120-dB stimulus was presented the first five times (Fig 7F). We did not detect significant differences in the PPI of the acoustic startle response in *Cox6a2*^{-/-} mice at prepulses of 72, 74, 78, and 86 dB (Fig 7G). In summary, these behavioral tests show that female *Cox6a2*^{-/-} mice showed hyperactivity in several behavioral paradigms that might be due to abnormalities in the molecular and functional properties of PV⁺ interneurons discovered above.

Patient carrying mutations in *COX6A2* exhibits low processing speed

We have provided comprehensive evidence that COX6A2 is required for the normal development and function of PV⁺ interneurons in mice. Furthermore, we showed a robust expression of COX6A2 in PV⁺ interneurons residing in the human prefrontal cortex. However, how these results might be translated into the effect of COX6A2 mutations in the human brain is unknown. Thus, we studied the intelligence and cognitive abilities of the only alive identified patient carrying mutations in COX6A2 (compound heterozygous, Ser39Arg, and Cys43Arg) (Inoue *et al*, 2019) (Fig 8A). To do so, we used the Wechsler Adult Intelligence Scale-III test (Wechsler, 1997) (Fig 8B). Interestingly, the full-scale intelligence quotient (IQ) and performance IQ of the patient were

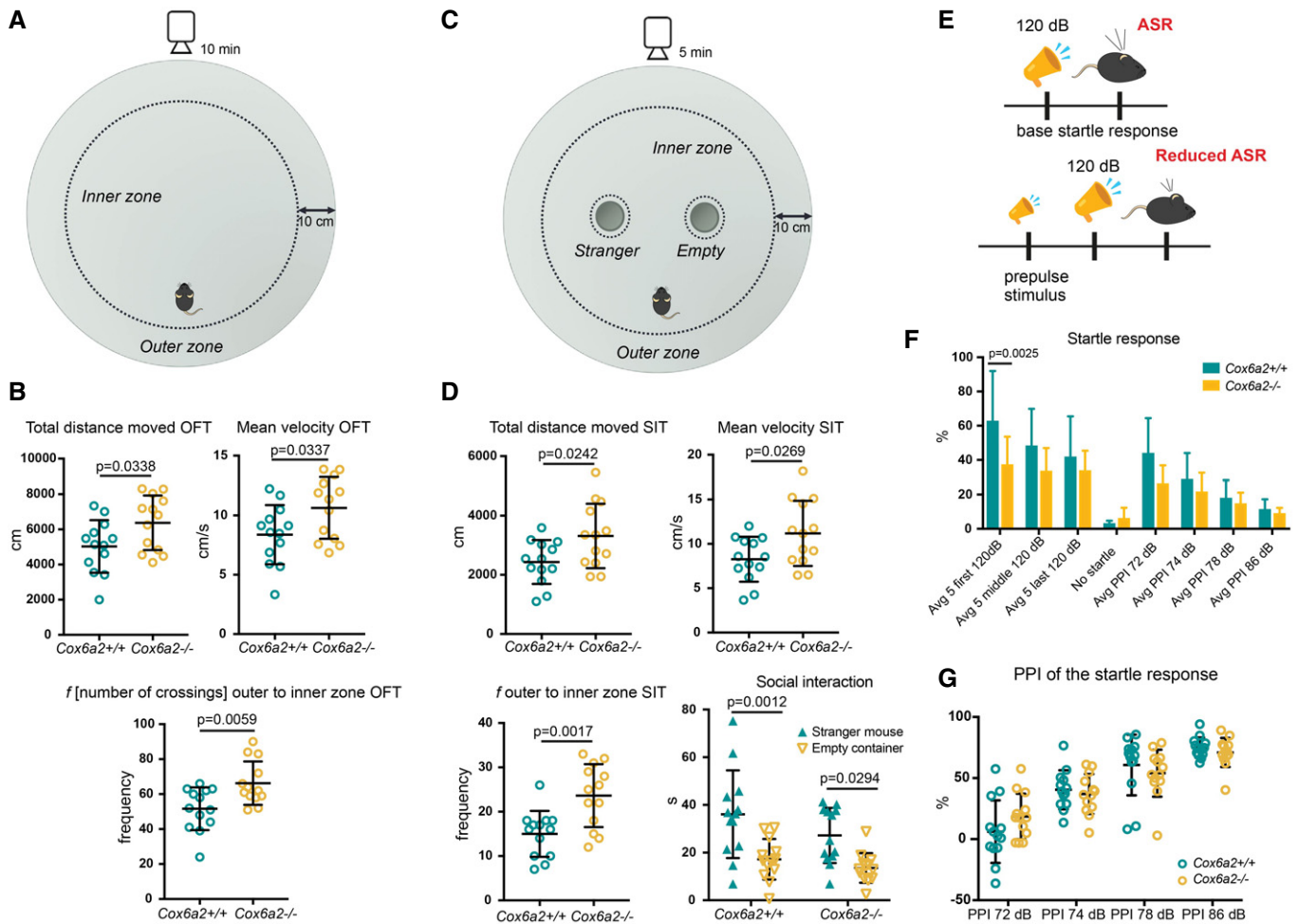


Figure 7. *Cox6a2*^{-/-} mice show behavioral alterations.

A Illustration of the arena used for the open-field test (OFT).
B In the OFT, *Cox6a2*^{-/-} mice traveled a longer distance and moved faster than WT mice. *Cox6a2*^{-/-} mice also moved more often from the outer zone to the inner zone of the arena. Two-tailed unpaired Student's *t*-tests.
C Illustration of the arena used for the social interaction test (SIT).
D In the SIT, *Cox6a2*^{-/-} mice also traveled a longer distance with higher mean velocity than WT mice. Additionally, both *Cox6a2*^{-/-} and WT mice spent more time exploring the container with the stranger mouse than the empty container. Total distance moved, mean velocity, and *f* (number of crossings) outer to inner zone: two-tailed unpaired Student's *t*-test. Social interaction: two-way ANOVA followed by Tukey's multiple comparisons test.
E Sensory gating was tested by the prepulse inhibition (PPI) of the acoustic startle response (ASR) test.
F The startle responses were significantly lower in *Cox6a2*^{-/-} mice when the loud stimulus (120 dB) was presented alone the first 5 times. Two-way ANOVA followed by Tukey's multiple comparisons tests.
G The PPI of the acoustic startle response was similar at all prepulses for *Cox6a2*^{-/-} and WT mice. Two-way ANOVA followed by Sidak's multiple comparisons tests.
 Data information: For all behavioral tests, *n* = 13 WT and 13 *Cox6a2*^{-/-} mice (~6–10 months old), all females. All error bars represent SD. For detailed statistical information, see Appendix Table S51–K.

found to be above average (Fig 8C). However, the score obtained for the processing speed (PS) was lower than average (Fig 8C), being around the PS of patients with mental/neurological abnormalities (Ojeda *et al*, 2012; Cook *et al*, 2018). Moreover, the large difference between PS (89 points) and full-scale IQ (111 points) further suggests that the patient might suffer a neurological condition since this is indicative of mental/neurological abnormalities in > 95% of patients (Calhoun & Mayes, 2005). Nevertheless, in spite of these initial observations of a potential contribution of *COX6A2* mutations to cognitive abnormalities in humans, the

identification and investigation of more individuals bearing *COX6A2* mutations are necessary to determine the link between mutations in *COX6A2* and human brain disorders.

Discussion

Fast-spiking PV⁺ interneurons are crucial components of cortical networks because they coordinate the firing activity of large ensembles of principal neurons, thereby generating brain oscillations

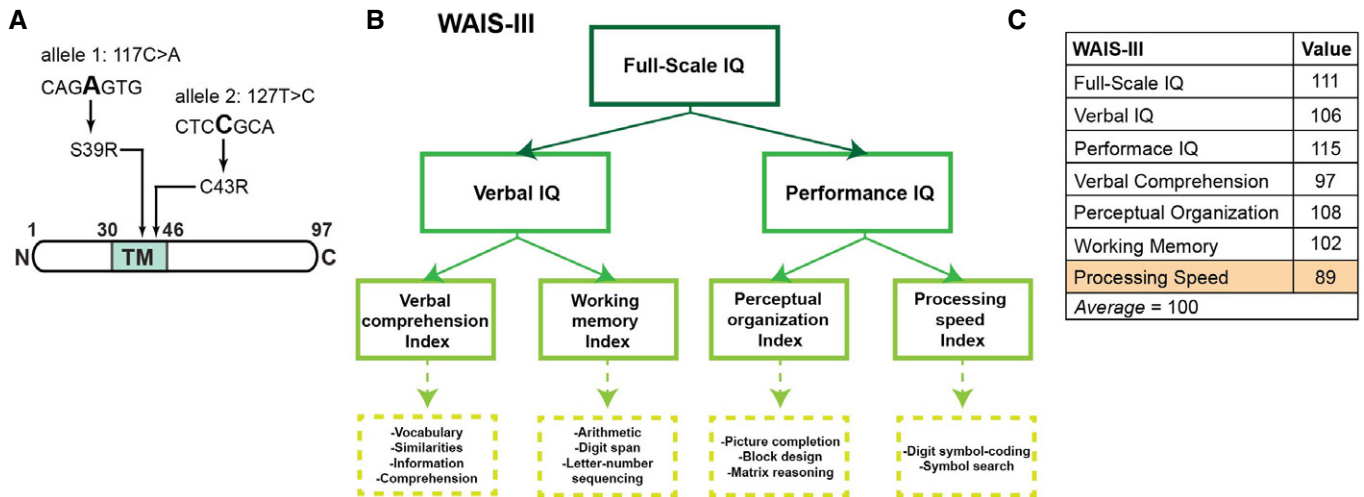


Figure 8. The effect of COX6A2 mutations on human intelligence and cognitive abilities.

- A The studied patient harbored compound heterozygous mutations in *COX6A2* gene (Inoue *et al*, 2019).
- B Scheme depicting the main functions analyzed by Wechsler Adult Intelligence Scale-III, the test that was used to evaluate the intelligence and cognitive abilities of the patient.
- C Values obtained by the patient. Orange indicates lower than average values.

(Cardin *et al*, 2009; Sohal *et al*, 2009) and maintaining a balance between cortical excitation and inhibition, processes required for brain computation and complex behaviors in mammals (Fries, 2009). Such unique functions of PV⁺ interneurons have been hypothesized to rely on a distinct metabolism optimized for high-frequency firing. Our data from mice demonstrate that PV⁺ interneurons express *Cox6a2*, a gene that encodes one of the two isoforms of COX6A subunit, which integrates CIV in the oxidative phosphorylation pathway. *Cox6a2* had been previously identified only in the heart and skeletal muscles (Kadenbach *et al*, 1982; Taanaman *et al*, 1993). Importantly, in the brain, *Cox6a2* expression is largely limited to PV⁺ interneurons, being virtually absent in other types of neurons and glia. In contrast, the gene encoding the other isoform of COX6A, *Cox6a1*, is ubiquitously expressed in the brain. PV⁺ interneurons lacking *Cox6a2* show lower parvalbumin expression, higher oxidative stress, and aberrant PNNs. *Cox6a2*^{-/-} PV⁺ interneurons exhibit impaired firing properties, form fewer synaptic contacts onto excitatory neurons, and show an abnormal morphology. Furthermore, in a key experiment, we showed a shift in energy balance of *Cox6a2*^{-/-} PV⁺ interneurons to lower ATP-to-ADP ratio. Altogether, these effects result in behavioral alterations in mice.

The unique fast-spiking properties of PV⁺ interneurons require a complex and coordinated work of the ion transport system that restores the intracellular ion concentrations after each action potential. This complex process must heavily rely on ATP. Importantly, COX6A2 is an ideal candidate to regulate ATP synthesis in PV⁺ interneurons, since COX6A2 but not COX6A1 is able to adjust the catalytic activity of CIV (Anthony *et al*, 1993; Frank & Kadenbach, 1996). Thus, studies on reconstituted COX6A2-containing CIV from the heart have shown that ADP stimulates CIV activity and low ATP-to-ADP ratio increases the proton transport efficiency of CIV (Anthony *et al*, 1993; Frank & Kadenbach, 1996). In contrast, COX6A1-containing CIV lacks ADP-dependent stimulation and

changes in the ATP-to-ADP ratio do not affect the efficiency of COX6A1-containing CIV (Huttemann *et al*, 1999). Strikingly, we found that PV⁺ interneurons lacking *Cox6a2* also exhibit a decreased expression of *Cox6a1*. Since the ubiquitously expressed COX6A1 isoform would normally substitute COX6A2 in CIV (Taanaman *et al*, 1993), reduced expression of *Cox6a1* in mutant PV⁺ interneurons could lead to the formation of fewer CIV, further disrupting the activity of the oxidative phosphorylation pathway.

We show that COX6A2 is essential for the maturation of the functional properties of PV⁺ interneurons over the period from P22 to P45. Interestingly, the impairment in the functional properties of *Cox6a2*^{-/-} PV⁺ interneurons was minor before ~ P30 and became more pronounced afterward. Thus, it seems that the effect of COX6A2 absence might accumulate over maturation, eventually hampering the normal development of PV⁺ interneurons. Such maturational delay resembles the impairment of PV⁺ interneurons that is observed in mental disorders (Gandal *et al*, 2012) and could lead to functional alterations in the neural networks controlled by PV⁺ interneurons, thereby contributing to their pathophysiology.

Selective expression of COX6A2 in PV⁺ interneurons also seems to protect them against oxidative stress. Reduced activity of CIV due to loss of COX6A2 has been shown to increase ROS production in the mitochondria (Quintens *et al*, 2013). Moreover, in this study, we observed higher oxidative DNA damage in PV⁺ interneurons lacking *Cox6a2* expression. In addition, it has been proposed that PV⁺ interneurons are more vulnerable to oxidative stress than other neurons possibly due to the higher metabolism required to sustain their electrophysiological properties (Steuillet *et al*, 2017). Thus, higher oxidative stress in PV⁺ interneurons in mouse models of mental disorders is associated with decreased expression of parvalbumin and GAD67, and loss of integrity of the PNNs that wrap them (Cabungcal *et al*, 2006, 2013b; Behrens *et al*, 2007). Interestingly, *Cox6a2*^{-/-} PV⁺ interneurons also show lower expression levels of parvalbumin, *Gad1* (GAD67) and *Gad2* (GAD65).

Furthermore, *Cox6a2*^{-/-} affects the integrity of PNNs surrounding PV⁺ interneurons. Thus, in addition to being essential for the maturation of PV⁺ interneurons, COX6A2 likely also protects them from increased ROS production and elevated oxidative stress.

Our animal behavior experiments showed that *Cox6a2*^{-/-} contributes to hyperactivity, whereas social and acoustic startle behaviors that are often affected in animal models of mental disorders such as schizophrenia (Meechan *et al*, 2009; Steullet *et al*, 2017) were not changed in *Cox6a2*^{-/-} mice. However, we analyzed behavior only in females and thus could not assess sex-specific differences in *Cox6a2*^{-/-}. In addition, based on limited human data, COX6A2 mutations might lead to cognitive abnormalities. One of the plausible explanations could be that the behavioral phenotype in *Cox6a2*^{-/-} mice is rather related to attention-deficit/hyperactivity disorder (ADHD). The low processing speed index that we identified for the patient with COX6A2 mutations was also previously associated with the ADHD phenotype (Cook *et al*, 2018). However, more comprehensive animal behavior and identification and investigation of a larger cohort of human patients bearing COX6A2 mutations are necessary to connect COX6A2 mutations to human neurodevelopmental disorders.

We found that the selective expression of *Cox6a2* in PV⁺ interneurons *in vivo* depends on two regulatory sites present in the *Cox6a2* promoter: MEF2- and E-box2-binding sites, which have been previously shown to regulate the expression of *Cox6a2* in myoblasts and fibroblasts *in vitro* (Wan & Moreadith, 1995). Interestingly, MEF2 also regulates parvalbumin expression and both MEF2 expression and parvalbumin expression are activity-dependent (Flavell *et al*, 2006). Recent studies have shown that PV⁺ interneurons exhibit different roles in memory acquisition depending on their high or low expression of PV, which under basal conditions correlates with the levels of MEF2 (Donato *et al*, 2013, 2015). Selective excitation/inhibition of high or low PV-expressing interneurons results in specific plasticity changes such that the former are recruited during memory acquisition, whereas the latter mediate memory consolidation. These MEF2-dependent effects might be mediated by adjusting *Cox6a2* expression according to the needs of PV⁺ interneurons in order to be integrated into the cortical and hippocampal networks.

Cox6a2 is a striking example of how regulation of gene expression can be adjusted not only according to the tissue needs but even to a particular cell type. Interestingly, the co-expression of *Cox6a2* and PV is conserved across mammals. Thus, it might be that during evolution the expression of energy-associated genes was optimized in fast-spiking interneurons, which shows how exceptionally important fast-spiking interneurons are for mammalian brain function.

Materials and Methods

Human subjects

The tissue samples from Brodmann areas 9 and 10 (BA9 and BA10), from 59-year-old man, and 69-year-old woman (both Caucasian, cause of death cardiovascular disorders), were provided by the Newcastle Brain Tissue Resource, and the immunohistochemical study was approved by the Danish Regional Ethics Committee.

Two patients with mutations in *Cox6a2* were identified in a previous study (Inoue *et al*, 2019). One of the patients died early after birth. The study of the second patient with compound heterozygous mutations in *Cox6a2* (Ser39Arg and Cys43Arg) was approved by the Institutional Review Board of the National Center of Neurology and Psychiatry and Chiba University Graduate School of Medicine. To access the clinical history of the patient, see Ref. (Inoue *et al*, 2019).

Animals

Cox6a2^{-/-} (Radford *et al*, 2002) and wild-type (WT) littermates, PV-EGFP (Meyer *et al*, 2002), PV-CRE (Hippenmeyer *et al*, 2005), GAD67-EGFP (Tamamaki *et al*, 2003), 5HT3AR-EGFP (Le Magueresse *et al*, 2011), and GIN-EGFP (Oliva *et al*, 2000) transgenic mice, all with C57BL/6 background, were used in the study.

Cox6a2^{fl/fl} mice were generated by Transgenic Core Facility of University of Copenhagen. Targeting of the DNA was done using the CRISPR/Cas9 technology which allowed precise and efficient targeting of this genetic region. Two guide RNAs were selected using CRISPOR tool (www.crispor.tefor.net):

gRNA1	CTGTTGAGCCCGCACATGGATGG
gRNA2	AAGGCCAATTTGAAGATTGCTGG

Both gRNA oligos were ordered from IDT and cloned into pX458 plasmid (Addgene; Cat #48138), as described in Ref. (Ran *et al*, 2013). dsDNA template was ordered from Thermo Scientific (GeneArt). The template, with a total size of 4,073 bp, was designed with 1,000 bp on each side of the loxP sites. The internal ribosome entry site (IRES) was placed at the 3' end of the *Cox6a2* coding sequence followed by the eGFP sequence. Both the genetic sequences of the *Cox6a2*, IRES, and eGFP were flanked by loxP sites placed in the same orientation (Appendix Fig S2A). F1.129S2; C57BL76N embryonic stem cells (mESCs) were transfected with the above-mentioned gRNA and donor template following the protocol described in Ref. (Yang *et al*, 2014). After one week in culture, 96 individual ESCs colonies were manually picked, disaggregated, and plated on a feeder cell layer in 96-well plates. This clone set was split in triplicates: Two of the copies were frozen, and the third was expanded up to confluent 24-well plate wells for DNA extraction and genotyping. ESC clones were genotyped by PCR using the following primers: seq-integration-fw (TGAGCAAAGACCCCAA CGAG) and seq-integration-rv (AGTGTTCCTACTACCAGTTCTGT CG), with expected size of the PCR amplicon 1,153 bp. Genotyping resulted in eight positive clones out of 96 (Appendix Fig S2B and C). The above positive clones were then tested for integration on the 5' side of the gene with a new set of primers: Cox-L-int-FW (CTCGGCTCCCAGGAGAGTAT) and Cox-L-int-RV (CCCGCACATA-TAATTCTGTATAGC) with expected size of the PCR amplicon 1,191 bp (Appendix Fig S2D). The sequence of the loxP sites was confirmed by amplification of 5' loxP site with a new set of primers, Cox-5check-Lox-FW (TGAAACACAGCAACAACCGAG) and Cox-5check-Lox-RV (TCTCCTTACCCAGTTCGAGA), and 3' loxP site by seq-integration-fw (TGAGCAAAGACCCCAAACCGAG) and seq-integration-rv (AGTGTTCCTACTACCAGTTCTGTTCG) primers (Appendix Fig S2B). Sequencing of the selected clones revealed the presence of the loxP sites in both the 5' and 3' locations of the gene. Once

the ESC clones carrying the mutation were identified by PCR, the selected clones were expanded and microinjected into morula stage C57BL6/N embryos, at a ratio of 5 cells per morula. The injected embryos were transferred to pseudopregnant recipient CD1 females. ESC clones #16 and #52 were injected. Clone #16 was injected into 24 embryos which gave rise to eight newborns, while clone #52 was injected into 24 embryos which resulted in four newborns. A total of 10 pups (six from clone #16 and all four from clone #52) turned out to be 100% ES-derived mice, assessed by coat color. At fertile age (2–3 months), sperm was extracted from these F0 males and IVF was performed on C57BL6/N oocytes in order to generate embryos. These embryos were sequentially washed and transferred to recipient females in order to rederive the line into the final mouse housing unit. F1 pups that were subsequently born were genotyped to confirm the transmission of the mutation.

In addition, one WT Wistar rat (2.5-month-old female) was used for the analysis. Mice (5–6 mice/cage) and the rat (2 rats/cage) were housed *ad libitum* in a standard 12-h light/dark cycle with a stable temperature of $23 \pm 1^\circ\text{C}$. Animal handling and sacrifice were carried out according to the Danish national legislation on animal experimentation (license number: 2015-15-0201-00762). Both male and female mice were used throughout the study unless otherwise specified. No sex-specific changes have been observed, which could be due to relatively small sample size to analyze sex-related differences, since sex-related differences were not the major aim of our study. Fixed rhesus monkey (1-year-old male) brain tissue samples were obtained from EUPRIM-Net Biobank.

Western blot analysis

Brain cortices were dissected from mouse brains at postnatal day 0 (P0), P5, P10, P20, and P60, and washed with phosphate-buffered saline (PBS, 1 \times , pH 7.4). The brains were weighted, minced with a blade, and resuspended in 10 volumes of lysis buffer (50 mM Tris-HCl pH 7.4; 150 mM NaCl; 0.5% SDS, 1% NP-40; 2 mM EDTA) supplemented with complete protease inhibitor cocktail (Roche). After 30-min incubating on ice, lysates were cleared by centrifugation at 25,000 *g* for 25 min. The protein concentration of lysates was determined by the Pierce 660 nm assay (Thermo Fisher). A total of 15 μg of protein per sample was loaded into a 10% tricine-SDS-PAGE for COX6A1, COX6A2, and cytochrome *c* oxidase 4, COX4, determination. Resolved proteins were transferred to a nitrocellulose membrane (Amersham Protran Premium, GE Healthcare) and incubated overnight (ON) at 4°C with primary antibodies against COX6A1, COX6A2, COX4, and glyceraldehyde 3-phosphate dehydrogenase (GAPDH; Appendix Table S4). After washing with PBS, the membrane was incubated with the corresponding secondary antibodies for 4 h at room temperature (RT; Appendix Table S4). The protein bands were visualized with SuperSignal West Pico System (Thermo Scientific) and X-ray film exposition.

Brain perfusion and tissue preparation for immunohistochemistry

Mice (several time points depending on the experiment; both sexes) and the rat (2.5-month-old female) were anesthetized by

intraperitoneal injection of ketamine (Richter Pharma AG, 200 mg/kg body weight) and xylazine (Biovet ApS, 10 mg/kg body weight). Once the paw pinch reflex was absent, rodents were transcardially perfused with approximately 5 ml of cooled (4°C) phosphate-buffered saline (PBS) followed by cooled 4% paraformaldehyde (PFA, Roth) at a flow rate of 8 ml/min for 4–8 min, depending on the size of the animal. Brains were removed and postfixed ON in 4% PFA at 4°C . A Leica VT1000 S vibratome (Leica, Germany) was used to slice the brains embedded in 4% agarose blocks to obtain 50- μm -thick serial coronal sections. Sections were then stored in PBS containing 0.01% NaN_3 at 4°C until further use.

Postfixed in 4% PFA serial brain sections from a rhesus monkey (1-year-old male) were provided by the EUPRIM-Net Biobank. The human (59-year-old man, 69-year-old woman) serial brain sections were provided by the Newcastle Brain Tissue Resource. They were fixed with formalin and embedded in paraffin before being shipped on dry ice.

Immunohistochemistry

Free-floating mouse, rat, and rhesus monkey brain sections were rinsed with PBS, blocked with 1% bovine serum albumin (BSA, PanReac AppliChem) and 1% normal goat serum (NGS, Life Technologies), and permeabilized with Triton X-100 in PBS (0.4% Triton X-100 for mouse and rat sections, and 1% for rhesus monkey sections, Sigma-Aldrich) for 1 h at RT. Sections were then incubated with primary antibodies (Appendix Table S4) ON at 4°C , rinsed in PBS, and incubated with the correspondent secondary antibodies (Appendix Table S4) for 4 h at RT. Both primary and secondary antibodies were diluted in 1% BSA, 1% NGS, and Triton X-100 in PBS (0.2% Triton X-100 for mouse and rat sections, and 0.6% for rhesus monkey sections). Sections were then rinsed with PBS, and nuclei were stained by incubation with 4',6-diamidino-2-phenylindole (DAPI, Invitrogen) for 10 min at RT. Finally, sections were rinsed with PBS and mounted on glass slides with mounting medium (Immu-Mount, Thermo Scientific). After drying out at RT ON in the darkness, glass slides were stored at 4°C until imaging. For the staining of PNNs, sections were first incubated with the dye WFA ON at 4°C , and after washing them with PBS, they were incubated with streptavidin and Alexa Fluor™ 647 conjugate for 4 h at RT (Appendix Table S4).

The human brain material was fixed by 4% paraformaldehyde, paraffin-embedded, sectioned, and stored by the brain bank. The received sections were dewaxed by incubation with double-distilled water (ddH_2O) at 60°C in a water bath for 15 min and rehydrated by sequential immersion in xylene (mixed isomers), 100% ethanol, 95% ethanol, 70% ethanol, 50% ethanol, and ddH_2O at RT. Sections were then submitted to antigen retrieval by incubation with Tris-EDTA-Tween 20 (pH 9) at 95°C in a water bath for 30 min. After cooling down, sections were permeabilized with 0.4% Triton X-100 in PBS for 10 min at RT. Subsequently, sections were blocked and further permeabilized with 1% BSA, 1% NGS, and 0.4% Triton X-100 in PBS for 1 h at RT before proceeding with the staining. The primary and secondary antibodies used were diluted in 1% BSA, 1% NGS, and 0.2% Triton X-100 in PBS. Importantly, the staining of each epitope was done individually to reduce to a minimum any unspecific signal, and sections were blocked

again before staining with the second set of primary and secondary antibody.

Identification of promoter sequences and transcription factors binding sites that regulate *Cox6a2* gene expression

Modules *Gene2Promoter* and *Genes and Genomes* from Genomatix (<https://www.genomatix.de>) were used to predict the putative position of the *Cox6a2* promoter in the genome of mouse, rat, rhesus monkey, and human genomes. Identification of the promoters upstream of the *Cox6a2* transcription start site (TSS) was performed using the UCSC Genome Browser. For each species, the predicted promoter site in closest proximity to *Cox6a2* TSS was selected for further analysis. These sequences were further analyzed using the Genomatix software module *Gene Regulator* that allowed for the mathematical prediction of transcription factor binding sites within a given promoter sequence. Following this approach, Genomatix identified two E-box transcription factor binding sites (E-box-1 and E-box2) and the MEF2 transcription factor binding site in the *Cox6a2* promoter with a high probability across the compared species. All modules used from Genomatix were utilized with standard presets suggested by the software.

Molecular cloning

To identify the role of E-box-2 and MEF2 transcription factor binding sites on *Cox6a2* expression *in vivo*, we amplified a 1,610 base pairs fragment of the *Cox6a2* promoter (*Cox6a2*prom) from the mouse genome using the following primers:

Cox6a2—forward: 5'-ATCCGAACCAAGCCCTTC-3'
Cox6a2—reverse: 5'-GTGGCAAGGATTGACG-3'

The amplified fragment was inserted upstream of EGFP into the AAV-CMV-EGFP vector, leading to the AAV-CMV-*Cox6a2*prom-EGFP vector. Next, the QuickChange II site-directed mutagenesis protocol (Agilent Technologies) was used to generate mutated replicates of the WT *Cox6a2*prom. In short, primers containing point mutations for the E-box2 and MEF2 transcription factor binding sites were designed based on the information obtained from Genomatix (see above) to alter the core transcription binding site in *Cox6a2*-prom (depicted in bold):

E-box2
 Predicted from Genomatix: 5'-tcaa**CAGG**tga-3'
 Mutated: 5'-tca**gTTTT**gga-3'
 MEF2
 Predicted from Genomatix: 5'aaagccccta**AAATAg**ccatcc-3'
 Mutated: 5'-aaagccccta**cCCCC**gcatcc-3'

The mutagenic primers were used to amplify the AAV-CMV-*Cox6a2*prom-EGFP vector by PfuTurbo DNA polymerase (Agilent Technologies). The template was then digested with Dpn I, and the obtained mutated vectors were used to transform competent bacteria.

To clone AAV-FLEX-CAG-PercevalHR, we replaced the EGFP cassette in AAV-CAG-FLEX-EGFP (Stratagene) by PercevalHR from FUGW-PercevalHR (Addgene #49083) (Tantama *et al*, 2013).

Recombinant virus production and titration

Recombinant adeno-associated viruses (AAVs) were produced as previously described (Khodosevich *et al*, 2013, 2014). Briefly, human embryonic kidney 293 cells (HEK 293 cells, Gibco) were plated on 15-cm tissue culture dishes (137 mm diameter, TPP) in growth medium (DMEM, 2 mM glutamine, 10% fetal calf serum, 1% penicillin/streptomycin; all from Gibco) and incubated at 37°C, 95% O₂/5% CO₂. Transfections were carried out when cells were ~80% confluent. One hour before transfection, the growth medium was substituted by transfection medium (DMEM, 2 mM glutamine). Cells were transfected using the calcium phosphate transfection method with the AAV plasmid (20 µg/plate) and the helper plasmids pDP1 and pDP2 (Grimm *et al*, 2003) (30 µg of each/plate). Plasmid DNA was mixed with CaCl₂ (final concentration 0.14 M) and 2× HBS (final concentration 280 mM NaCl, 1.5 mM NaH₂PO₄ [×2 H₂O], pH 6.96), and directly added to cells in transfection medium (1 ml/plate). Cells were incubated for 4–5 h at 37°C and at a low CO₂ concentration (3%). Subsequently, the plasmid DNA mix was removed and cells were washed with preheated PBS at 37°C followed by incubation with growth medium for 60–72 h at 37°C and 95% O₂/5% CO₂. Finally, cells were harvested and the virus was purified using heparin affinity column HiTrap Heparin HP (GE Healthcare). The genomic titers were determined by quantitative PCR using primers designed to amplify EGFP/PercevalHR with the LightCycler 480 II (Roche).

Stereotactic injection of recombinant viruses into the brain of mice

Brain injections of AAV-CMV-*Cox6a2*prom-EGFP (or mutated *Cox6a2* promoter versions) were performed in 2- to 3-month-old WT mice and AAV-FLEX-CAG-PercevalHR in 15-day-old PV-CRE and PV-CRE;*Cox6a2*^{fl/fl} mice as previously described (Garcia-Gonzalez *et al*, 2017; Korshunova *et al*, 2020). Briefly, mice were placed in a stereotactic apparatus (Angle Two, Leica) and anesthetized by continuous inhalation of isoflurane (Virbac, 1.0–1.5 flow rate). Once the paw pinch reflex was absent, the head and jaw of the animal were fixed and the area on the top of the head was thoroughly cleaned with 70% ethanol and sprayed with xylocaine (AstraZeneca, 10 mg/dose) to provide local anesthesia. In 1–2 min, a longitudinal incision across the skin following the middle line of the head was made with scissors to open the skull. The Bregma was visualized, and the coordinates for the Bregma were set to zero. The coordinates for injection were set to (from Bregma) anterior/posterior 0 mm, medial/lateral +1.5 mm or –1.5 mm, dorsal/ventral +1 mm for AAV-CMV-*Cox6a2*prom-EGFP, and anterior/posterior 0 mm, medial/lateral +2.0 mm or –2.0 mm, dorsal/ventral +1.7 mm for AAV-FLEX-CAG-PercevalHR. The whole in the skull above the injection site was made by the 27G syringe needle (BD). The 10-µl NanoFil syringe (WPI) with 36G blunt needle was fixed at the stereotactic holder and loaded with the AAV. The tip of the NanoFil syringe was placed at the desired coordinates, and 1 µl of the AAV was delivered in the somatosensory cortex. Following the injection, the skin was sealed and mice were allowed to recover from the anesthesia on a heating pad for 15–20 min and subsequently moved to postsurgical cages. As post-operative analgesia, we used carprofen, subcutaneously, 5 mg/kg,

single dose ~ 50 μ l; and buprenorphine, subcutaneously, 0.1 mg/kg, single dose ~ 50 μ l. Mice were under observation over 48 h after the surgery, period during which they received a high caloric dietary supplement (DietGel[®] Boost, Clear H₂O) together with regular food pellets. Mice injected by AAV-CMV-Cox6a2prom-EGFP (or mutated Cox6a2 promoter versions) were sacrificed ~ 3 weeks postinjection by transcardial perfusion with 4% PFA; mice injected by AAV-FLEX-CAG-PercevalHR were sacrificed ~ 3 weeks postinjection by transcardial perfusion with aCSF, as described in the section Electrophysiological recordings.

Image acquisition and analysis

Immunolabeled brain sections were imaged with a confocal microscope (Leica SP8, Leica Microsystems), and quantifications were performed using FIJI (Schindelin *et al*, 2012) unless otherwise specified. For detailed sample size and statistical information, see Appendix Tables S5.

COX6A2 and PV double-positive cells in mice (P13 and P60, both sexes, corresponding to the onset of parvalbumin expression young adult), rats (2.5-month-old female adult), rhesus monkey (1-year-old male), and human (59-year-old man and 69-year-old woman) samples were quantified in the region of interest (ROI). The ROI in mice was in the somatosensory (SS) and motor (MT) cortices (spanning from layer I to layer VI, ~ 640 \times 640 μ m, vertical \times horizontal), in the striatum (in the dorsal part, 320 \times 320 μ m), and in the rostral part of the hippocampus (HI; covering the entire CA1, CA2, CA3, and the dentate gyrus, DG). Cortical layers were differentiated using the neuronal nuclear antigen NeuN. Quantifications were carried out in both hemispheres. The ROI in rats was in the SS and MT cortices, covering layers I–VI (640 \times 640 μ m, both hemispheres). The ROI in rhesus monkey was in the SS cortex, covering layers II–IV (640 \times 640 μ m, one hemisphere). The ROI in humans was in the Brodmann areas 9 and 10 (BA9, BA10) covering all cortical layers across the entire section supplied.

The rest of the quantifications were performed in mice only. Cortical layers were differentiated using the neuronal nuclear antigen NeuN. COX6A2- and EGFP-double-positive cells in GAD67-EGFP, 5HT3AR-EGFP, and GIN-EGFP mice were quantified in layers I–VI (640 \times 640 μ m, both hemispheres) in the SS and MT cortices at P60. The density of PV⁺ interneurons (P60 and P180) in the SS and MT cortices was quantified in the ROI that spanned all cortical layers (2,300 \times 550 μ m, both hemispheres).

The mean fluorescence intensity (MFI) of parvalbumin was analyzed in the SS cortex at P60, mainly in cells in the layers IV–VI due to higher density of PV⁺ interneurons in the deeper layers. The intensity was measured as mean gray value, and all images for quantifications have been acquired with the same parameters. The cells with MFI below 40 were considered as background.

The number of PV⁺ interneuron synaptic contacts onto principal neurons was quantified at P60 in all cortical layers of the SS cortex. Cell bodies of principal neurons were identified using NeuN labeling, and the number of PV⁺ synaptic puncta around the cell bodies was quantified in *z* stacks of confocal images obtained using 0.5- μ m steps spanning the whole-cell body of the principal neuron of interest.

The MFI of the 8-hydroxy-2'-deoxyguanosine (8-OHdG) antibody labeling was automatically measured in PV⁺ interneurons located in the cortical layer IV of the SS and MT cortices at P60

using Imaris (Bitplane AG). The same procedure was followed for the measurement of the MFI of WFA antibody labeling around PV⁺ interneurons at P60.

The quantification of PV and EGFP double-positive cells after injection of AAVs expressing EGFP under the control of intact or mutated *Cox6a2* promoters was carried out across the whole SS cortex, avoiding the area immediately adjacent to the injection site.

Electrophysiological recordings

Electrophysiological recordings were performed in double-blind manner using brain sections from WT and *Cox6a2*^{-/-} PV-EGFP transgenic mice that were 3–6 weeks old at the time of the experiment. PV⁺ interneurons were identified in slices based on EGFP expression. The time period of recordings (P22–P45) corresponds to the late maturational period of PV⁺ interneurons (Okaty *et al*, 2009; Miyamae *et al*, 2017). The recorded cells were later split into two equal parts of maturational period, P22–P33 and P34–P45; for explanations, see the Results section.

On the day of the experiment, mice were deeply anesthetized by an intraperitoneal injection of ketamine (MSD, 100 mg/kg body weight) and xylazine (ScanVet, 10 mg/kg body weight) and transcardially perfused with cooled (4°C) choline chloride artificial cerebrospinal fluid (cc-aCSF; 110 mM choline chloride, 25 mM NaHCO₃, 1.25 mM NaH₂PO₄, 2.5 mM KCl, 0.5 mM CaCl₂, 7 mM MgCl₂, 25 mM glucose, 11.6 mM ascorbic acid, 3.1 mM sodium pyruvate; all from Sigma-Aldrich) saturated with carbogen (95% O₂, 5% CO₂). The head of the mouse was cut off as soon as the perfusion was completed and submerged in cool cc-aCSF saturated with carbogen. The brain was extracted, and the cerebellum and olfactory bulbs were removed. The caudal side of the brain was glued to a metal stage and placed in the slicing chamber filled with cool cc-aCSF saturated with carbogen. Brains were sliced into 300- μ m-thick coronal sections using a VT1200 vibratome (Leica Biosystems, Germany) and subsequently transferred to regular aCSF (125 mM NaCl, 25 mM NaHCO₃, 1.25 mM NaH₂PO₄, 2.5 mM KCl, 0.5 mM CaCl₂, 7 mM MgCl₂, 25 mM glucose; all from Sigma-Aldrich) saturated with carbogen at 37°C for 5 min. The slices were then maintained at RT until recording.

Brain slices were placed in a recording chamber under the objective of an upright BX51WI microscope (Olympus Life Science Europa, Germany). The chamber was continuously perfused with aCSF saturated with carbogen and heated to 30–32°C using a bath controller V heating system (Luigs & Neumann, Germany). Patch electrodes (resistance of 2–9 M Ω) were pulled on a P-87 flaming brown pipette puller (Sutter Instruments Co., USA) and were filled with 122 mM K-gluconate, 5 mM Na₂ATP, 2.5 mM MgCl₂, 0.0003 mM CaCl₂, 5.6 mM Mg-gluconate, 5 mM K-Hepes, 5 mM H-Hepes, 1 mM EGTA, 10 mM biocytin (all from Sigma-Aldrich), and 0.01 mM Alexa Fluor 568 hydrazide (Invitrogen; pH 7.4). The patch pipette was positioned on a three-axis motorized micromanipulator (Luigs & Neumann, Germany) connected to a CV-7B Headstage (Molecular Devices, Sunnyvale CA, USA). EGFP-labeled cortical PV⁺ interneurons were identified by epifluorescence and were recorded with the whole-cell configuration patch-clamp technique in current-clamp mode. Recordings were made using a MultiClamp 700B amplifier (Molecular Devices, Sunnyvale CA, USA). Data were sampled at 10 kHz, sent to a computer via a 1440A digitizer

(Molecular Devices, Sunnyvale CA, USA), and displayed by means of Clampex software (Molecular Devices, Sunnyvale CA, USA).

The input resistance was calculated as the slope of the linear fit of the current–voltage relationship between -10 and $+10$ mV. The spike threshold was determined as the first positive peak above 10^{12} mV/s³ present on the third derivative of the voltage trace in a 1-ms time window preceding the peak of the action potential (Henze & Buzsáki, 2001). The upstroke of action potential was calculated as the maximum of the first derivative of the membrane potential occurring in a 1-ms time window before the peak. The maximal firing rate was determined by applying incremental 2-s depolarizing current pulses. For all cells tested, we observed that the frequency reached a plateau value. The ability of interneurons to sustain repetitive firing was checked by applying 30-s depolarizing current pulses of increasing intensities.

Data analysis was performed using Matlab 2016a (MathWorks, USA), Python 3.6 (Python Software Foundation), and Clampfit 10.7 (Molecular Devices, USA). Statistics and figures were done with Prism 7 (GraphPad Software, USA) and OriginPro 2017 (OriginLab, USA). Data are presented as mean \pm standard deviation of the mean (SD). Normality was tested using Shapiro–Wilk test. Normally distributed samples were compared with the two-tailed independent *t*-test. Samples that did not pass the normality test were compared using the nonparametric Mann–Whitney test.

Reconstruction of neuronal morphology

Once the electrophysiological recordings were completed, PV⁺ interneurons were filled with biocytin (Sigma-Aldrich). The recorded sections were postfixed in 4% PFA and stored at 4°C until further processing. Sections were stained following the immunohistochemistry protocol described above. Briefly, the sections were blocked and permeabilized with 1% BSA, 1% NGS, and 0.4% Triton X-100 for 1 h at RT, followed by incubation with the rabbit anti-EGFP antibody ON at 4°C. On the following day, sections were incubated with Streptavidin Texas Red™ conjugate, which binds to biocytin, and Alexa Fluor 488 donkey anti-rabbit secondary antibody. Z stacks of stained neurons were obtained by confocal microscopy, and neuronal morphology was reconstructed using Imaris 7.6 (Bitplane). A total of 24 WT PV⁺ interneurons and 19 *Cox6a2*^{fl/fl} PV⁺ interneurons were reconstructed and analyzed. Based on neuronal morphology, all reconstructed PV⁺ interneurons were classified as basket cells. For each reconstructed neuron, we quantified dendritic length, full branch depth (maximum number of branches between the soma and a terminal point), and dendritic tree complexity (number of dendrite intersections with concentric spheres that extend from the cell body) by 3D Sholl analysis (Sholl, 1953).

Live-cell imaging of PercevalHR in PV⁺ interneurons

Approximately 3 weeks after being injected with AAV-FLEX-CA G-PercevalHR, four PV-CRE and six PV-CRE;*Cox6a2*^{fl/fl} mice were transcardially perfused, and their brains were processed as described in the section Electrophysiological recordings. Both PV-CRE and PV-CRE;*Cox6a2*^{fl/fl} mice were 35–45 days old at the time of the experiment. Brain slices were placed in the recording chamber under the 40 \times objective of a Bergamo II two-photon microscope (Thorlabs) equipped with a laser Coherent Chameleon Ultra 2. The

chamber was permanently perfused with aCSF at 30°C saturated with carbogen (95% O₂, 5% CO₂). To avoid any minor displacement of the brain slices during the recordings, they were mounted on lens cleaning tissue paper (Sigma-Aldrich) and immobilized with a platinum harp. The fluorescence emission of PercevalHR in PV⁺ interneurons was imaged at the excitation wavelengths 840 and 930 nm to estimate ATP-to-ADP ratio within these cells as described before (Tantama et al, 2013). All recordings lasted 5 min. Only PV⁺ interneurons present in the SS cortex on layers IV–VI were imaged, and the damaged area surrounding the injection site was avoided. The mean fluorescence intensity (MFI) of PercevalHR in PV⁺ interneuron somata was measured over the time series using FIJI (Schindelin et al, 2012). The ratiometric ATP-to-ADP signals were determined as Fhigh-to-Flow: MFI at 930 nm (conformational state of PercevalHR bound to ATP is maximally excited at 930 nm)/MFI at 840 nm (conformational state of PercevalHR bound to ADP is maximally excited at 840 nm) (Tantama et al, 2013).

Fluorescence-activated cell sorting of PV⁺ interneurons and RNA sequencing

A total of four WT and six *Cox6a2*^{fl/fl} PV-EGFP mice were sacrificed by decapitation at P15, and their brains were collected in ice-cold aCSF (120 mM NaCl, 25 mM NaHCO₃, 2.5 mM KCl, 1.25 mM NaH₂PO₄, 2 mM CaCl₂, 1 mM MgCl₂, and 10 mM glucose) supplemented with 500 μ M ascorbic acid and saturated with carbogen (95% O₂, 5% CO₂). The entire cortex (i.e., from prefrontal to visual area) was micro-dissected on ice and dissociated for 30 min at 37°C in 1 ml of papain solution (Papain Dissociation System, Worthington LK003150) containing 500 μ M ascorbic acid. During the incubation, the tissue was mechanically disrupted by gentle pipetting every 10 min to obtain a single-cell suspension. To remove debris and nondissociated tissue fragments, the cell suspension was filtered through a 70- μ m cell-strainer and subsequently collected by centrifugation (300 g for 5 min). The collected pellet was resuspended in 1 ml resuspension buffer (900 μ l EBSS buffer, 100 μ l ovalbumin inhibitor, 50 μ l DNase I [2 μ g/ μ l]) and layered over 2 ml ovalbumin inhibitor. Subsequently, the cell suspension was centrifuged at 150 g for 6 min and the resulting cell pellet was resuspended in 300 μ l fluorescence-activated cell sorting (FACS) buffer (4.7 ml HBSS buffer, 250 μ l BSA [20%], 50 μ l DNase I [2 μ g/ μ l]). EGFP-positive and EGFP-negative single cells were bulk-collected separately in 350 μ l RLT lysis buffer containing 1% β -mercaptoethanol using FACS Aria I or III (BD) with 100 μ m nozzle. Subsequent to collection, samples were vortexed, centrifuged, and stored at -80° C until further processing.

RNA extractions were performed using Qiagen RNeasy Kit following the manufacturer's instructions. A total of 250 pg RNA per sample with a RIN value of 7.5–10 was mixed with 0.2 μ l RNase inhibitor (40 U/ μ l), 1 μ l oligo-dT (10 μ M, /5Bios/AAGCAGTG GTATCAACGCAGAGTACT₃₀VN/3/), and 1 μ l dNTP mix (10 μ M, 2.5 μ M each). Samples were then centrifuged and incubated at 72°C for 3 min, and cDNA libraries were prepared by the Smart-seq2 method (Picelli et al, 2014) with some custom-made modifications. In short, each sample was mixed with 5.3 μ l of reverse transcription master mix containing 0.5 μ l SuperScript III (200 U/ μ l), 0.25 μ l RNase inhibitor (40 U/ μ l), 2 μ l 5 \times first-strand buffer, 2 μ l 5M

betaine, 0.06 μ l 1 M MgCl₂, and 0.5 μ l 100 mM DTT. The plate containing samples was centrifuged for 1 min at 1,000 g and incubated for reverse transcription as follows: 42°C–90:00, 42°C–hold, 42°C–12:20, 10 cycles (50°C–2:00, 42°C–2:00), 39°C–10:00, 70°C–15:00, and 4°C–hold. After 90 min of the incubation at 42°C, the plate was taken out of the thermocycler, and 0.4 μ l of TSO (12.5 μ M, /5Biosg/AAGCAGTGGTATCAACGCAGAGTACATrGrG+G/3/) was added to each sample and incubation continued for another 12:20. Following reverse transcription, 15 μ l cDNA enrichment master mix containing 12.5 μ l 2 \times KAPA HiFi HotStart ReadyMix, 0.25 μ l (10 μ M, /5Biosg/AAGCAGTGGTATCAACGCAGAGT/3/), and 2.25 μ l water was added to each first-strand reaction. The plate was centrifuged and incubated as follows: 98°C–3:00, five cycles (98°C–0:20, 60°C–4:00, 72°C–6:00), six cycles (98°C–0:20, 64°C–0:30, 72°C–6:00), five cycles (98°C–0:20, 67°C–0:15, 72°C–7:00), 72°C–10:00, and 4°C–hold. The amplified cDNA was purified using AMPure XP beads at a ratio 1:1.

Illumina Nextera XT sequencing libraries were prepared according to the manufacturer's instructions using 350 pg input cDNA per sample and 12 cycles of library enrichment PCR. The concentration of cDNA libraries was determined by Qubit 3.0 according to the manufacturer's instructions, and the average library fragment length was assessed using the DNA HS assay on the Bioanalyser (Agilent). Each library was individually normalized to a final concentration of 2 nM, and all libraries were combined to yield a 2 nM library pool. Equimolar library pools were denatured according to Illumina's recommendations and sequenced on an Illumina NextSeq500 (single end, 75 bp) at an average depth of 10 mio reads/library. Raw data are available at ArrayExpress (<http://www.ebi.ac.uk/arrayexpress>) with accession code E-MTAB-7879.

RNA-seq data processing

Fastq files were trimmed with Trimmomatic 0.32 (Bolger *et al*, 2014) using parameters HEADCROP:12 LEADING:3 TRAILING:3 SLIDINGWINDOW:4:15 MINLEN:25. Trimmed fastq files were aligned to GRCm38/mm10 (RefSeq assembly accession: GCF_000001635.20) using STAR-2.5.1a (Dobin *et al*, 2013). Reads were quantified using featureCounts (Liao *et al*, 2014) 1.5.1 using the ensembl GTF Mus_musculus.GRCm38.86.gtf.

To analyze differential gene (DE) expression between WT and *Cox6a2*^{-/-} PV interneurons, the count matrix generated previously by feature counts was loaded into DESeq2 (Love *et al*, 2014). Libraries were normalized and DE genes between WT ($n = 4$) and *Cox6a2*^{-/-} ($n = 6$) samples were calculated using the DESeq and results function selecting genes with $P_{adj} < 0.05$. Differentially expressed genes between WT and *Cox6a2*^{-/-} samples were plotted into heat maps using z-scores.

Pathway enrichment analysis was performed on the DE genes between WT and *Cox6a2*^{-/-} samples, with GO biological process, cellular component, and molecular-function terms within clusterProfiler version 3.4.4 (Yu *et al*, 2012) by using a Benjamini–Hochberg-adjusted P value ≤ 0.05 as the significance threshold.

Genes belonging to GO terms: 0006091 “generation of precursor metabolites and energy” and 0070888 “E-box binding” were extracted from Ref. (Tasic *et al*, 2016).

Behavioral tests

The behavioral performance of 13 WT and 13 *Cox6a2*^{-/-} female mice was assessed. Female mice were chosen due to economic reasons and since sex-specific differences were not the major focus of the study. The estrus cycle was not checked. At the time of the first behavioral test, mice were 5–6 months old. The cohort was selected from littermates derived from heterozygous *Cox6a*^{+/-} breedings. The following behavioral paradigms have been implemented: the OFT, the SIT, and the PPI of the acoustic startle response test. C57BL/6J female mice have been shown to exhibit a stable behavior throughout the four phases of the estrous cycle in several behavioral tests (Meziane *et al*, 2007). Therefore, they represent an adequate population of animals for the purposes of the study. To reduce potential external stressors, mice were not disturbed for 3 days before the start of a training session/test. Additionally, mice were allowed to habituate to the behavioral room for 1 h the day before the start of a training session/test and on the same day the trainings/test were performed. This also applied to the stranger mice used in the SIT. All training sessions/tests were performed during the light phase.

Mice were submitted to the OFT and SIT sequentially in the same arena, which consisted of a brightly lit 120-cm-wide circular arena surrounded by 60-cm height walls. In the OFT, mice were recorded for 10 min, which provided us information about their locomotor activity and level of anxiety-like behavior. Importantly, the OFT was also used to habituate test mice to the arena, reducing novelty-related locomotor hyperactivity that could potentially affect social interaction in the SIT that was performed right after the OFT. Mice have a natural tendency to interact with an unfamiliar rodent over a novel inanimate object. Thus, in the SIT, two identical cylindrical containers that allowed visual, olfactory, and tactile interactions between the test and stranger mice were placed in the center of the arena. A female stranger mouse of approximately the same age and body weight as the test mouse was placed in one of the cylinders. The other container remained empty. Test mice activity was analyzed for 5 min. To assess their level of sociability, we measured the time test mice spent interacting, both directly and indirectly, with the stranger mouse and the empty cylinder. By indirect interaction, we refer to the time the animal's nose was within 2 cm of the cylinders and pointing toward them. Videos of mice performing the OFT and SIT were analyzed using the EthoVision XT video tracking tool (Noldus, Netherlands).

PPI of the acoustic startle response was measured the week after the end of OFT and SIT using the SR-Lab™ SDI startle response system (San Diego Instruments, INC. Europe) as before (Hougaard *et al*, 2005). Briefly, mice were placed in 3.6-cm-wide tubes in calibrated chambers where a continuous white background noise of 70 dB was present. A piezoelectric accelerometer transduced the displacement of the tubes in response to movements of the animal. Mice were acclimatized in the tube for 5 min before sessions started. The session started and finished with five startle trials, each of which consisted of a stimulus of 120 dB and 40 ms of duration. Then, 35 trials were delivered in a semi-randomized order: 10 trials of 120 dB; 20 trials of 120 dB preceded by a prepulse of 72, 74, 78, or 86 dB (five of each type; denoted PPI72, PPI74, PPI78, and PPI86, respectively); and five trials with white background noise only. Tube movements were registered for 100 ms after the start of the

acoustic stimulus. The average response over the 100 ms of each trial was calculated, and the average response for the trials of the same level of prepulse (e.g., the five startle trials preceded by a prepulse of 72 dB) was obtained. These values were used to calculate the PPI, which is defined as the percent reduction in the acoustic startle reaction after presenting a prepulse compared to the acoustic startle response to the 120-dB noise pulse without the preceding prepulse: %PPI = 100 – [(Average response to Prepulse + 120 dB noise pulse)/Average response to 120 dB noise pulse] × 100.

Cognitive assessment of the human subject carrying *Cox6a2* mutations

The evaluation of the cognitive abilities and intelligence of the human patient carrying mutations in *Cox6a2* was performed using the Wechsler Adult Intelligence Scale (WAIS)-III (Wechsler, 1997). This intelligence quotient (IQ) test provides scores for verbal IQ and performance IQ. Verbal IQ is assessed by verbal comprehension and working memory tasks, while performance IQ is evaluated by tasks related to perceptual organization and processing speed. The total score obtained is called full-scale IQ.

Statistics

Statistical analysis of the data collected from the immunohistochemistry experiments, reconstructed neurons, and behavioral tests were performed with Prism 7.0 (GraphPad software). Normality of data distribution was analyzed by D'Agostino and Shapiro–Wilk's tests. When comparing two populations, normally distributed data were analyzed by two-tailed Student's *t*-test, whereas non-normally distributed data were analyzed by two-tailed Mann–Whitney test. More than two populations were compared using one-way ANOVA. When comparing two parameters between two or more populations, a two-way ANOVA with Sidak or Tukey's correction was carried out. *F* test was used to compare the variances. Females and males were analyzed together and the graphs represent joint sex data, except for the behavioral tests, where only female mice were used. For detailed statistical information, see Appendix Table S5.

Data availability

The RNA-seq data generated in this study have been deposited in the ArrayExpress database at EMBL-EBI under accession number E-MTAB-7879 (<http://www.ebi.ac.uk/arrayexpress/experiments/E-MTAB-7879>).

Expanded View for this article is available online.

Acknowledgements

We would like to thank Prof. Hannah Monyer and Dr. Anne Herb for providing mouse brains from 5HT3A-EGFP and GIN transgenic mouse lines. We thank Newcastle Brain Tissue Resource for supplying the human tissue samples. We also wish to thank the Microscopy and Flow Cytometry BRIC Core Facilities, Dr. Gopal Karemore for helping on the analysis of immunohistochemistry data, and members of the Khodosevich laboratory for constructive discussions

relating to this study. The work was supported by Novo Nordisk Hallas-Møller Investigator Grant (NNF16OC0019920), Lundbeck-NIH Brain Initiative Grant (2017-2241) and DFF-Forskningsprojekt1 (8020-00083B) to KK, Owensenske Foundation and Agnes and Poul Friis Foundation to JFP, and Russian Foundation for Basic Research (18-29-07002) to SL.

Author contributions

KK conceived the study. BS-M performed most of the experiments under KK supervision and PercevalHR *in vivo* imaging under J-FP supervision. UP and AT performed RNA sequencing of PV⁺ interneurons. UP performed *Cox6a2* promoter analysis and RT-PCR for *Cox6a1/2* mRNA. NWH and AM performed electrophysiology under the supervision of JFP. SD analyzed single cell and bulk RNA sequencing data. SAL performed Western blot analysis of COX6A2 expression under the supervision of PK. IK produced recombinant viruses. KF performed experiments for a patient with mutations in *COX6A2* under the supervision of SN. KSH supervised behavioral experiments. BIA contributed to metabolism experiments. PPAM provided *Cox6a2* knockout mice. KK and BSM wrote the manuscript. All authors edited the manuscript.

Conflict of interest

The authors declare that they have no conflict of interest.

References

- Anthony G, Reimann A, Kadenbach B (1993) Tissue-specific regulation of bovine heart cytochrome-c oxidase activity by ADP via interaction with subunit VIa. *Proc Natl Acad Sci USA* 90: 1652–1656
- Behrens MM, Ali SS, Dao DN, Lucero J, Shekhtman G, Quick KL, Dugan LL (2007) Ketamine-induced loss of phenotype of fast-spiking interneurons is mediated by NADPH-oxidase. *Science* (80-) 318: 1645–1647
- Behrens MM, Sejnowski TJ (2009) Does schizophrenia arise from oxidative dysregulation of parvalbumin-interneurons in the developing cortex? *Neuropharmacology* 57: 193–200
- Bolger AM, Lohse M, Usadel B (2014) Trimmomatic: a flexible trimmer for Illumina sequence data. *Genome Res* 30: 2114–2120
- Cabungcal JH, Nicolas D, Kraftsik R, Cuénod M, Do KQ, Hornung JP (2006) Glutathione deficit during development induces anomalies in the rat anterior cingulate GABAergic neurons: relevance to schizophrenia. *Neurobiol Dis* 22: 624–637
- Cabungcal JH, Steullet P, Kraftsik R, Cuenod M, Do KQ (2013a) Early-life insults impair parvalbumin interneurons via oxidative stress: reversal by N-acetylcysteine. *Biol Psychiatry* 73: 574–582
- Cabungcal JH, Steullet P, Morishita H, Kraftsik R, Cuenod M, Hensch TK, Do KQ (2013b) Perineuronal nets protect fast-spiking interneurons against oxidative stress. *Proc Natl Acad Sci USA* 110: 9130–9135
- Cabungcal JH, Steullet P, Kraftsik R, Cuenod M, Do KQ (2019) A developmental redox dysregulation leads to spatio-temporal deficit of parvalbumin neuron circuitry in a schizophrenia mouse model. *Schizophr Res* 213: 96–106
- Caillard O, Moreno H, Schwaller B, Llano I, Celio MR, Marty A (2000) Role of the calcium-binding protein parvalbumin in short-term synaptic plasticity. *Proc Natl Acad Sci USA* 97: 13372–13377
- Calhoun SL, Mayes SD (2005) Processing speed in children with clinical disorders. *Psychol Sch* 42: 333–343
- Cardin JA, Carlen M, Meletis K, Knoblich U, Zhang F, Deisseroth K, Tsai LH, Moore CI (2009) Driving fast-spiking cells induces gamma rhythm and controls sensory responses. *Nature* 459: 663–667

- Cho RY, Konecky RO, Carter CS (2006) Impairments in frontal cortical synchrony and cognitive control in schizophrenia. *Proc Natl Acad Sci USA* 103: 19878–19883
- Chung DW, Fish KN, Lewis DA (2016) Pathological basis for deficient excitatory drive to cortical parvalbumin interneurons in schizophrenia. *Am J Psychiatry* 173: 1131–1139
- Cook NE, Braaten EB, Surman CBH (2018) Clinical and functional correlates of processing speed in pediatric attention-deficit/hyperactivity disorder: a systematic review and meta-analysis. *Child Neuropsychol* 24: 598–616
- Dobin A, Davis CA, Schlesinger F, Drenkow J, Zaleski C, Jha S, Batut P, Chaisson M, Gingeras TR (2013) STAR: ultrafast universal RNA-seq aligner. *Bioinformatics* 29: 15–21
- Donato F, Rompani SB, Caroni P (2013) Parvalbumin-expressing basket-cell network plasticity induced by experience regulates adult learning. *Nature* 504: 272–276
- Donato F, Chowdhury A, Lahr M, Caroni P (2015) Early- and late-born parvalbumin basket cell subpopulations exhibiting distinct regulation and roles in learning. *Neuron* 85: 770–786
- Enwright JF, Sanapala S, Foglio A, Berry R, Fish KN, Lewis DA (2016) Reduced labeling of parvalbumin neurons and perineuronal nets in the dorsolateral prefrontal cortex of subjects with schizophrenia. *Neuropsychopharmacology* 41: 2206–2214
- Fishell G, Rudy B (2011) Mechanisms of inhibition within the telencephalon: 'where the wild things are'. *Annu Rev Neurosci* 34: 535–567
- Flavell SW, Cowan CW, Kim TK, Greer PL, Lin Y, Paradis S, Griffith EC, Hu LS, Chen C, Greenberg ME (2006) Activity-dependent regulation of MEF2 transcription factors suppresses excitatory synapse number. *Science (80-)* 311: 1008–1012
- Frank V, Kadenbach B (1996) Regulation of the H⁺/e⁻-stoichiometry of cytochrome c oxidase from bovine heart by intramitochondrial ATP/ADP ratios. *FEBS Lett* 382: 121–124
- Fries P (2009) Neuronal gamma-band synchronization as a fundamental process in cortical computation. *Annu Rev Neurosci* 32: 209–224
- Gandal MJ, Nesbitt AM, McCurdy RM, Alter MD (2012) Measuring the maturity of the fast-spiking interneuron transcriptional program in autism, schizophrenia, and bipolar disorder. *PLoS ONE* 7: e41215
- García-González D, Khodosevich K, Watanabe Y, Rollenhagen A, Lubke JHR, Monyer H (2017) Serotonergic projections govern postnatal neuroblast migration. *Neuron* 94: 534–549.e9
- Grimm D, Kay MA, Kleinschmidt JA (2003) Helper virus-free, optically controllable, and two-plasmid-based production of adeno-associated virus vectors of serotypes 1 to 6. *Mol Ther* 7: 839–850
- Grossman LI, Rosenthal NH, Akamatsu M, Erickson RP (1995) Cloning, sequence analysis, and expression of a mouse cDNA encoding cytochrome c oxidase subunit VIa liver isoform. *Biochim Biophys Acta* 1260: 361–364
- Gulyas AI, Buzsáki G, Freund TF, Hirase H (2006) Populations of hippocampal inhibitory neurons express different levels of cytochrome c. *Eur J Neurosci* 23: 2581–2594
- Henze DA, Buzsáki G (2001) Action potential threshold of hippocampal pyramidal cells *in vivo* is increased by recent spiking activity. *Neuroscience* 105: 121–130
- Hippenmeyer S, Vrieseling E, Sigrist M, Portmann T, Laengle C, Ladle DR, Arber S (2005) A developmental switch in the response of DRG neurons to ETS transcription factor signaling. *PLoS Biol* 3: e159
- Hougaard KS, Andersen MB, Hansen AM, Hass U, Werge T, Lund SP (2005) Effects of prenatal exposure to chronic mild stress and toluene in rats. *Neurotoxicol Teratol* 27: 153–167
- Hu H, Gan J, Jonas P (2014) Fast-spiking, parvalbumin+ GABAergic interneurons: from cellular design to microcircuit function. *Science* 345: 1255263–1255263
- Huttemann M, Frank V, Kadenbach B (1999) The possible role of isoforms of cytochrome c oxidase subunit VIa in mammalian thermogenesis. *Cell Mol Life Sci* 55: 1482–1490
- Inoue M, Uchino S, Iida A, Noguchi S, Hayashi S, Takahashi T, Fujii K, Komaki H, Takeshita E, Nonaka I et al (2019) COX6A2 variants cause a muscle-specific cytochrome c oxidase deficiency. *Ann Neurol* 86: 193–202
- Kadenbach B, Hartmann R, Glanville R, Buse G (1982) Tissue-specific genes code for polypeptide VIa of bovine liver and heart cytochrome c oxidase. *FEBS Lett* 138: 236–238
- Kann O, Papageorgiou IE, Draguhn A (2014) Highly energized inhibitory interneurons are a central element for information processing in cortical networks. *J Cereb Blood Flow Metab* 34: 1270–1282
- Kann O (2016) The interneuron energy hypothesis: implications for brain disease. *Neurobiol Dis* 90: 75–85
- Khodosevich K, Lazarini F, von Engelhardt J, Kaneko H, Lledo PM, Monyer H (2013) Connective tissue growth factor regulates interneuron survival and information processing in the olfactory bulb. *Neuron* 79: 1136–1151
- Khodosevich K, Jacobi E, Farrow P, Schulmann A, Rusu A, Zhang L, Sprengel R, Monyer H, von Engelhardt J (2014) Coexpressed auxiliary subunits exhibit distinct modulatory profiles on AMPA receptor function. *Neuron* 83: 601–615
- Korshunova I, Rhein S, García-González D, Stölting I, Pfisterer U, Barta A, Dmytriyeva O, Kirkeby A, Schwaninger M, Khodosevich K (2020) Genetic modification increases the survival and the neuroregenerative properties of transplanted neural stem cells. *JCI Insight* 5: e126268
- Le Magueresse C, Alfonso J, Khodosevich K, Arroyo Martin AA, Bark C, Monyer H (2011) 'Small axonless neurons': postnatally generated neocortical interneurons with delayed functional maturation. *J Neurosci* 31: 16731–16747
- Le Magueresse C, Monyer H (2013) GABAergic interneurons shape the functional maturation of the cortex. *Neuron* 77: 388–405
- Liao Y, Smyth GK, Shi W (2014) featureCounts: an efficient general purpose program for assigning sequence reads to genomic features. *Bioinformatics* 30: 923–930
- Love MI, Huber W, Anders S (2014) Moderated estimation of fold change and dispersion for RNA-seq data with DESeq2. *Genome Biol* 15: 550
- Lovelace JW, Rais M, Palacios AR, Shuai XS, Bishay S, Popa O, Pirbhoy PS, Binder DK, Nelson DL, Ethell IM et al (2020) Deletion of Fmr1 from forebrain excitatory neurons triggers abnormal cellular, EEG, and behavioral phenotypes in the auditory cortex of a mouse model of fragile X syndrome. *Cereb Cortex* 30: 969–988
- Lu J, Tucciarone J, Lin Y, Huang ZJ (2014) Input-specific maturation of synaptic dynamics of parvalbumin interneurons in primary visual cortex. *Proc Natl Acad Sci USA* 111: 16895–16900
- Mancarci BO, Toker L, Tripathy SJ, Li B, Rocco B, Sibille E, Pavlidis P (2017) Cross-laboratory analysis of brain cell type transcriptomes with applications to interpretation of bulk tissue data. *eNeuro* 4: 1–20
- Marin O (2012) Interneuron dysfunction in psychiatric disorders. *Nat Rev Neurosci* 13: 107–120
- Meechan DW, Tucker ES, Maynard TM, LaMantia A (2009) Diminished dosage of 22q11 genes disrupts neurogenesis and cortical development in a mouse model of 22q11 deletion/DiGeorge syndrome. *Proc Natl Acad Sci USA* 106: 16434–16445

- Meyer AH, Katona I, Blatow M, Rozov A, Monyer H (2002) *In vivo* labeling of parvalbumin-positive interneurons and analysis of electrical coupling in identified neurons. *J Neurosci* 22: 7055–7064
- Meziane H, Ouagazzal A-M, Aubert L, Wietrzyk M, Krezel W (2007) Estrous cycle effects on behavior of C57BL/6J and BALB/cByJ female mice: implications for phenotyping strategies. *Genes Brain Behav* 6: 192–200
- Minzenberg MJ, Firl AJ, Yoon JH, Gomes GC, Reinking C, Carter CS (2010) Gamma oscillatory power is impaired during cognitive control independent of medication status in first-episode schizophrenia. *Neuropsychopharmacology* 35: 2590–2599
- Miyamae T, Chen K, Lewis DA, Gonzalez-Burgos G (2017) Distinct physiological maturation of parvalbumin-positive neuron subtypes in mouse prefrontal cortex. *J Neurosci* 37: 4883–4902
- Mukherjee A, Carvalho F, Eliez S, Caroni P (2019) Long-lasting rescue of network and cognitive dysfunction in a genetic schizophrenia model. *Cell* 178: 1387–1402.e14
- Muñoz-Manchado AB, Bengtsson Gonzales C, Zeisel A, Munguba H, Bekkouche B, Skene NG, Lönnberg P, Ryge J, Harris KD, Linnarsson S et al (2018) Diversity of Interneurons in the dorsal striatum revealed by single-cell RNA sequencing and PatchSeq. *Cell Rep* 24: 2179–2190.e7
- Ojeda N, Peña J, Schretlen DJ, Sánchez P, Aretouli E, Elizagárate E, Ezcurra J, Gutiérrez M (2012) Hierarchical structure of the cognitive processes in schizophrenia: the fundamental role of processing speed. *Schizophr Res* 135: 72–78
- Okaty BW, Miller MN, Sugino K, Hempel CM, Nelson SB (2009) Transcriptional and electrophysiological maturation of neocortical fast-spiking GABAergic interneurons. *J Neurosci* 29: 7040–7052
- Oliva AA Jr, Jiang M, Lam T, Smith KL, Swann JW (2000) Novel hippocampal interneuronal subtypes identified using transgenic mice that express green fluorescent protein in GABAergic interneurons. *J Neurosci* 20: 3354–3368
- Patrizi A, Awad PN, Chattopadhyaya B, Li C, Di Cristo G, Fagiolini M (2020) Accelerated hyper-maturation of parvalbumin circuits in the absence of MeCP2. *Cereb Cortex* 30: 256–268
- Paul A, Crow M, Raudales R, He M, Gillis J, Huang ZJ (2017) Transcriptional architecture of synaptic communication delineates GABAergic neuron identity. *Cell* 171: 522–539.e20
- Picelli S, Faridani OR, Bjorklund AK, Winberg G, Sagasser S, Sandberg R (2014) Full-length RNA-seq from single cells using Smart-seq2. *Nat Protoc* 9: 171–181
- Quintens R, Singh S, Lemaire K, De Bock K, Granvik M, Schraenen A, Vroegrijk IO, Costa V, Van Noten P, Lambrechts D et al (2013) Mice deficient in the respiratory chain gene Cox6a2 are protected against high-fat diet-induced obesity and insulin resistance. *PLoS ONE* 8: e56719
- Radford NB, Wan B, Richman A, Szczepaniak LS, Li J-L, Li K, Pfeiffer K, Schagger H, Garry DJ, Moreadith RW (2002) Cardiac dysfunction in mice lacking cytochrome-c oxidase subunit VIaH. *Am J Physiol Hear Circ Physiol* 282: 726–733
- Ran FA, Hsu PD, Wright J, Agarwala V, Scott DA, Zhang F (2013) Genome engineering using the CRISPR-Cas9 system. *Nat Protoc* 8: 2281–2308
- Rudy B, Fishell G, Lee S, Hjerling-Leffler J (2011) Three groups of interneurons account for nearly 100% of neocortical GABAergic neurons. *Dev Neurobiol* 71: 45–61
- Schindelin J, Arganda-Carreras I, Frise E, Kaynig V, Longair M, Pietzsch T, Preibisch S, Rueden C, Saalfeld S, Schmid B et al (2012) Fiji: an open-source platform for biological-image analysis. *Nat Methods* 9: 676–682
- Sholl DA (1953) Dendritic organization in the neurons of the visual and motor cortices of the cat. *J Anat* 87: 387–406
- Sohal VS, Zhang F, Yizhar O, Deisseroth K (2009) Parvalbumin neurons and gamma rhythms enhance cortical circuit performance. *Nature* 459: 698–702
- Sokoloff L (1960) The metabolism of the central nervous system *in vivo*. In *Handbook of Physiology, Section 1, Neurophysiology*, Field J, Magoun HW, Hall VE, eds, Vol. 3, pp. 1843–1864. Washington DC: American Physiological Society
- Steuillet P, Cabungcal JH, Coyle J, Didriksen M, Gill K, Grace AA, Hensch TK, LaMantia AS, Lindemann L, Maynard TM et al (2017) Oxidative stress-driven parvalbumin interneuron impairment as a common mechanism in models of schizophrenia. *Mol Psychiatry* 22: 936–943
- Taanaman JW, Hall RE, Tang C, Marusich MF, Kennaway NG, Capaldi RA (1993) Tissue distribution of cytochrome c oxidase isoforms in mammals. Characterization with monoclonal and polyclonal antibodies. *Biochim Biophys Acta* 1225: 95–100
- Tamamaki N, Yanagawa Y, Tomioka R, Miyazaki J, Obata K, Kaneko T (2003) Green fluorescent protein expression and colocalization with calretinin, parvalbumin, and somatostatin in the GAD67-GFP knock-in mouse. *J Comp Neurol* 467: 60–79
- Tantama M, Martinez-Francois JR, Mongeon R, Yellen G (2013) Imaging energy status in live cells with a fluorescent biosensor of the intracellular ATP-to-ADP ratio. *Nat Commun* 4: 2550
- Tasic B, Menon V, Nguyen TN, Kim TK, Jarsky T, Yao Z, Levi B, Gray LT, Sorensen SA, Dolbeare T et al (2016) Adult mouse cortical cell taxonomy revealed by single cell transcriptomics. *Nat Neurosci* 19: 335–346
- Tremblay R, Lee S, Rudy B (2016) GABAergic interneurons in the neocortex: from cellular properties to circuits. *Neuron* 91: 260–292
- Vasistha NA, Pardo-Navarro M, Gasthaus J, Weijers D, Müller MK, García-González D, Malwade S, Korshunova I, Pfisterer U, Von Engelhardt J et al (2019) Maternal inflammation has a profound effect on cortical interneuron development in a stage and subtype-specific manner. *Mol Psychiatry* <https://doi.org/10.1038/s41380-019-0539-5>
- Wan B, Moreadith RW (1995) Structural characterization and regulatory element analysis of the heart isoform of cytochrome c oxidase VIa. *J Biol Chem* 270: 26433–26440
- Wechsler D (1997) *WAIS-III/WMS-III technical manual harcourt brace*. San Antonio, TX: Psychological Corporation
- Wen TH, Afroz S, Reinhard SM, Palacios AR, Tapia K, Binder DK, Razak KA, Ethell IM (2018) Genetic reduction of matrix metalloproteinase-9 promotes formation of perineuronal nets around parvalbumin-expressing interneurons and normalizes auditory cortex responses in developing Fmr1 knock-out mice. *Cereb Cortex* 28: 3951–3964
- Yang H, Wang H, Jaenisch R (2014) Generating genetically modified mice using CRISPR/Cas-mediated genome engineering. *Nat Protoc* 9: 1956–1968
- Yu G, Wang L-G, Han Y, He Q-Y (2012) clusterProfiler: an R package for comparing biological themes among gene clusters. *OMICS J* 16: 284–287